Symmetries and gaits for Purcell's three-link microswimmer model

Emiliya Gutman and Yizhar Or

***Abstract*—Robotic locomotion typically involves using gaits — periodic changes of kinematic shape, which induce net motion of the body in a desired direction. An example is robotic microswimmers, which are inspired by motion of swimming microorganisms. One of the most famous theoretical models of a microswimmer is Purcell's planar three-link swimmer, whose structure possesses two axes of symmetry. Several works analyzed gaits for robotic three-link systems based on body-fixed velocity integrals. Using this approach, finite motion in desired directions can only be obtained approximately. In this work we propose gaits which are based on analysis of the system's structural symmetries, and generate exact motion along principal directions without net rotation. Another gait that produces almost pure rotation is presented, and bounds on the small-amplitude residual translation are obtained by using perturbation expansion. Next, the theory is extended to more realistic swimmers which have only one symmetry axis. Gaits for such swimmers which generate net translation are proposed, and their small-amplitude motion is analyzed using perturbation expansion. The theoretical results are demonstrated by using numerical simulations and conducting controlled motion experiments with a robotic macro-swimmer prototype in a highly viscous fluid.**

I. Introduction

Locomotion is defined as the ability of a living creature, a mobile robot or a vehicle to propel itself by means of physical interaction with the surrounding environment. A typical way of locomotion is using *gaits*, which are periodic changes in the internal shape, in order to generate net motion of the body. In the literature of robotics and nonlinear control, locomotion systems and their gaits are usually analyzed using the concept of geometric mechanics [1], [2], which involves differential and Riemannian geometry and group theory, or by using notions of nonholonomic systems and nonlinear control theory [3]–[5]. One of the well-studied theoretical models of locomotion systems is microswimmers [6], which are greatly inspired by motion of swimming microorganisms [7]. This research topic has recently gained increasing interest due to its promising potential for development of robotic microswimmers [8], [9], which are planned to be used for biomedical applications such as minimally invasive surgery and targeted drug delivery [10], [11].

Swimming at the micro-scale is governed by low Reynolds number hydrodynamics, where viscous drag effects are dominating while inertial effects are negligible [12]. The fluid is governed by Stokes equations and its interaction with the swimmer is quasistatic, making the dynamics time-invariant. This enables formulation of the equations of motion as first-order ordinary differential equations which fit well into the framework of the geometric theory of locomotion [1], [2], [5]. In the literature on nonlinear control systems, several works study controllability aspects of microswimming systems [13], [14], while other works analyze their geometric structure [6], [15]. In the general physics and fluid mechanics literature, although theoretical formulation of microswimming dates back to the pioneering work of G. I. Taylor in 1951 [16], the classical paper of E. M. Purcell on "Life at low Reynolds number" [17] is one of the most cited works in the field, while later works studied various theoretical models of simple microswimmers [18], [19]. Purcell proposed a simple microswimmer model which is composed of three elongated links connected by two revolute joints, whose angles $\phi_1(t), \phi_2(t)$ are prescribed in a periodic gait, See Fig. 1. The swimmer possesses two axes of symmetry, and Purcell stated, without providing any explicit formulation, that under the square-shaped gait shown in Fig. 1(b) the net motion is along the middle link's longitudinal axis due to symmetry considerations. The proof of this statement was left as an exercise to the reader in [17], and one of the objectives of this paper is to provide this proof as part of a systematic analysis of symmetries and gaits for this swimmer. Only 26 years after Purcell's paper, the dynamics of the three-link swimmer was explicitly formulated by Becker *et al* [20] by using slender body theory [21], [22]. In later works, Tam and Hosoi [23] studied optimization of gaits for generation of maximal displacement or energetic efficiency, and Giraldi *et al* [24] studied similar problems from perspective of optimal control. Avron and Raz [25] studied the swimmer's symmetries and proposed a simplified symmetric version of the model which displays one-dimensional linear motion only.

Several works studied the control of large robotic swimmers in just the opposite physical extreme of "perfect fluid" where drag effects are neglected while inertial effects are dominating [26]–[28]. Remarkably, in these systems the structure of the resulting control system is very similar to that of microswimmers, where both systems are governed by linear relations between shape velocities and body velocities, known as *principal connections* [2]. Several other types of robotic locomotion systems were analyzed using similar concepts, where the principal connections are typically imposed by nonholonomic no-slip constraints of wheels or blades, as in the classical examples of Chaplygin's sleigh [2], snakeboard [29], and roller-racer [30]. While these systems are affected by combination of principal connections and evolution of momentum, the *kinematic snake* model studied in [31], which consists

E. Gutman and Y. Or are with the Faculty of Mechanical Engineering, Technion - Israel Institute of Technology. izi@technion.ac.il

of three links supported by wheeled axles, is governed only by principal connections due to kinematic no-slip constraints. Thus, its equations of motion share a similar structure as the three-link swimmer, either in perfect or in highly viscous fluid[1].

Recent works on analyzing gaits for robotic three-link systems have used the concept of *body-velocity integral* (BVI), in which the velocities expressed in a body-fixed frame are integrated in order to find the net body motion under a given gait [32]. The main disadvantage of this method is that one cannot directly relate BVI to finite motion of the body due to non-commutativity of the Lie group $SE(2)$ of translation and rotation in the plane. In [27], the semidirect-product structure of $SE(2)$ is exploited for generating gaits that achieve a desired net rotation, without controlling the resulting net translation. The works of Hatton and Choset [28], [33] proposed a systematic choice of optimal coordinates that minimize the approximation error of BVI. Many of the works on three-link systems have made intuitive use of their structural symmetries for generation of symmetric gaits. This dates back to Purcell's original square gait (Fig. 1(b)), and to Tam and Hosoi [23] who limited their search of optimal gaits to those with two particular axes of symmetry that lead to net translation in longitudinal direction. Avron and Raz [25] identified symmetries of Purcell's swimmer in terms of body-fixed velocities, which were not extended to finite body motion. Shammas and Choset [31] proposed gaits with certain symmetries for the kinematic snake model, but their symmetry arguments were again limited to body velocities only.

The goal of this paper is to complement all these works mentioned above by presenting a systematic analysis of the symmetries of Purcell's three link microswimmer model and their effect on generating gaits with particular symmetries in order to achieve desired net motion. Unlike many works that study optimal gaits which maximize displacement or minimize time or energy expenditure (cf. [13], [14], [23], [29], [34]), and are typically limited to numerical search, our work focuses only on generating gaits that result in net motion along a desired direction, and make exact claims based on symmetry arguments. We propose two generic types of symmetric gaits that achieve net translation in longitudinal and transversal directions. Then we propose another type of gait that achieves almost pure net rotation, and find bounds on the residual translation under small amplitudes by using perturbation expansion. Next, we analyze more realistic models of three-link swimmers that possess only one axis of symmetry. We propose gaits that generate pure net translation, and obtain the scaling of small-amplitude motion by using perturbation expansion. The theoretical results are verified via numerical simulations and also demonstrated experimentally by presenting motion measurement of a macro-scale robotic swimmer in a highly viscous fluid. While our work focuses on Purcell's swimmer, the results are fairly general and apply to any three-link locomotion system with similar symmetries.

[1]Interestingly, the kinematic snake suffers from singularity at symmetric configurations where the joint angles satisfy $\phi_1 = \phi_2$ (see Fig. 1(a)) since the two nonholonomic constraints become linearly dependent. This singularity does not occur at the three-link swimmer models.

We do not make use of terminology of differential geometry and group theory, and all the symmetries are formulated in terms of algebraic operations on matrices in $SE(2)$ that represent planar rigid-body transformations. This makes our analysis highly accessible to a broad audience of the robotics community.

The organization of the paper is as follows. The next section introduces Purcell's swimmer model and formulates its dynamic equations. In section III the swimmer's symmetries of body velocities are formulated. In addition, reflection operators on trajectories of shape changes are defined, and their effect on symmetries of finite motion is analyzed. In section IV three different types of symmetric gaits are studied, which generate net translation in principal directions and almost pure rotation. Section V analyzes the swimmer's motion scaling under small-amplitude gaits. In section VI, gaits for swimmers with only one axis of symmetry are analyzed. Section VII presents experimental results of a macro-scale robotic swimmer prototype. The concluding section discusses limitations of the results and proposes some possible directions for extension of the research. An Appendix contains technical details and proofs of all theorems. Supplemntary material contains video movies of three gaits of the robotic swimmer and animations of numerical simulations of the swimmers under several gaits.

II. Problem formulation

We now formulate the dynamics of Purcell's three link swimmer. The swimmer, depicted in Fig. 1(a), consists of three slender rigid links whose lengths are l_0, l_1 and l_2. The links are connected by two rotary joints whose angles are denoted by ϕ_1 and ϕ_2. The planar motion of the swimmer is described by coordinates $\mathbf{q} = (x, y, \theta)^T$ which give the position of the center of the middle link and its orientation angle. The shape of the swimmer is described by the two joint angles $\boldsymbol{\phi} = (\phi_1, \phi_2)^T$.

First, we express the kinematic relations of links' velocities. The velocity of the i^{th} link is described by the linear velocity of its center $\mathbf{v}_i$ and the link's angular velocity ω_i, which are augmented in the vector $\mathbf{V}_i = (\mathbf{v}_i, \omega_i) \in \mathbb{R}^3$. The velocity $\mathbf{V}_i$ is related to the body velocity $\dot{\mathbf{q}}$ and shape velocity $\dot{\boldsymbol{\phi}}$ as:

$$\mathbf{V}_i = \mathbf{T}_i(\mathbf{q}, \boldsymbol{\phi})\dot{\mathbf{q}} + \mathbf{E}_i(\mathbf{q}, \boldsymbol{\phi})\dot{\boldsymbol{\phi}}. \tag{1}$$

The matrices $\mathbf{T}_i(\mathbf{q}, \boldsymbol{\phi})$ and $\mathbf{E}_i(\mathbf{q}, \boldsymbol{\phi})$ for $i = 0, 1, 2$ are given by:

$$\mathbf{T}_0 = \begin{bmatrix} 1 & 0 & 0 \\ 0 & 1 & 0 \\ 0 & 0 & 1 \end{bmatrix}, \ \mathbf{E}_0 = \begin{bmatrix} 0 & 0 \\ 0 & 0 \\ 0 & 0 \end{bmatrix}$$

$$\mathbf{T}_1 = \begin{bmatrix} 1 & 0 & -0.5l_o \sin\alpha_o - 0.5l_1 \sin\alpha_1 \\ 0 & 1 & 0.5l_o \cos\alpha_o + 0.5l_1 \cos\alpha_1 \\ 0 & 0 & 1 \end{bmatrix}, \mathbf{E}_1 = \begin{bmatrix} -0.5l_1 \sin\alpha_1 & 0 \\ 0.5l_1 \cos\alpha_1 & 0 \\ 1 & 0 \end{bmatrix}$$

$$\mathbf{T}_2 = \begin{bmatrix} 1 & 0 & 0.5l_o \sin\alpha_o + 0.5l_2 \sin\alpha_2 \\ 0 & 1 & -0.5l_o \cos\alpha_o - 0.5l_2 \cos\alpha_2 \\ 0 & 0 & 1 \end{bmatrix}, \mathbf{E}_2 = \begin{bmatrix} 0 & -0.5l_2 \sin\alpha_2 \\ 0 & 0.5l_2 \cos\alpha_2 \\ 0 & -1 \end{bmatrix}, \tag{2}$$

where $\alpha_o = \theta$, $\alpha_1 = \theta + \phi_1$ and $\alpha_2 = \theta - \phi_2$.

It is assumed that the fluid motion is governed by Stokes equations [12]. In order to formulate the dynamic equation of the swimmer we use Resistive Force Theory (RFT) [21], [22]. Under this theory, the viscous drag force $\mathbf{f}_i$ and torque τ_i on

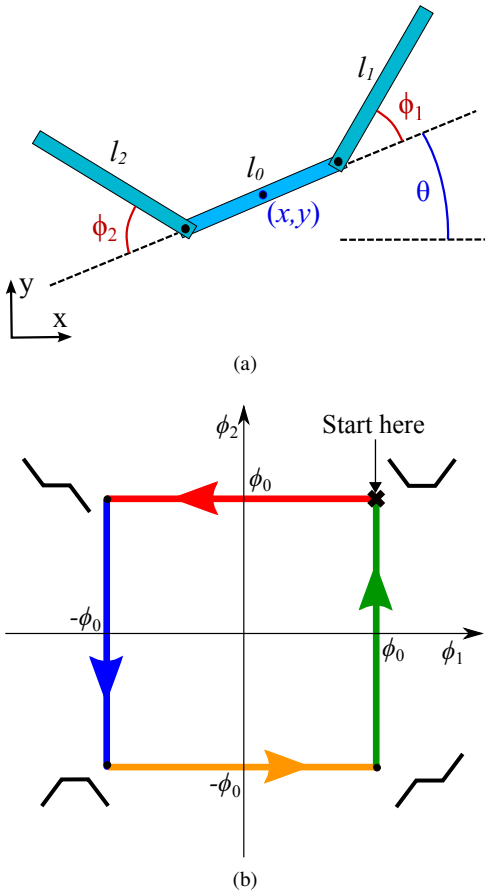

Fig. 1: (a) Purcell's three-link swimmer model. (b) Square gait of Purcell's swimmer that describes the changes of the swimmer's joint angles in $\phi_1 - \phi_2$ plane which generate net motion in x direction.

the i^{th} slender link under planar motion are proportional to its linear and angular velocities according to the relations:

$$\begin{aligned} \mathbf{f}_i &= -c_t^{(i)} l_i (\mathbf{v}_i \cdot \mathbf{t}_i)\mathbf{t}_i - c_n^{(i)} l_i (\mathbf{v}_i \cdot \mathbf{n}_i)\mathbf{n}_i \\ \tau_i &= -\frac{1}{12} c_n^{(i)} l_i^3 \omega_i, \end{aligned} \tag{3}$$

Where l_i is the link's length, $\mathbf{t}_i = (\cos\alpha_i, \sin\alpha_i)^T$ is a unit vector in its axial direction, and $\mathbf{n}_i = (-\sin\alpha_i, \cos\alpha_i)^T$ is a unit vector in the normal direction. The resistance coefficients in (3) for the normal and axial directions are given by $c_n^{(i)} = 2c_t^{(i)} = 4\pi\mu/\log(l_i/a)$ where a is the radius of the links and μ is the fluid's viscosity. It is assumed that the hydrodynamic interaction between the links of the swimmer is negligible. Denoting the vector of forces and torques on the i^{th} link as $\mathbf{F}_i = (\mathbf{f}_i, \tau_i)$, the relations (3) can be written in matrix form as

$$\mathbf{F}_i = -\boldsymbol{\mathcal{R}}_i(\mathbf{q}, \boldsymbol{\phi})\mathbf{V}_i, \text{ where}$$

$$\boldsymbol{\mathcal{R}}_i(\mathbf{q}, \boldsymbol{\phi}) = c_t^{(i)} l_i \begin{bmatrix} 1+\sin^2\alpha_i & -\cos\alpha_i \sin\alpha_i & 0 \\ -\cos\alpha_i \sin\alpha_i & 1+\cos^2\alpha_i & 0 \\ 0 & 0 & \frac{1}{6} l_i^2 \end{bmatrix} \tag{4}$$

The matrix $\boldsymbol{\mathcal{R}}_i$ in (4) is called the resistance tensor, and is known to be symmetric and positive definite for any finite-sized body [12]. Using the kinematic relations (1), the net hydrodynamic force and torque acting on the swimmer's body are given by

$$\mathbf{F}_b = \sum_{i=0}^{2} \mathbf{T}_i^T \mathbf{F}_i = -\sum_{i=0}^{2} \mathbf{T}_i^T \boldsymbol{\mathcal{R}}_i (\mathbf{T}_i \dot{\mathbf{q}} + \mathbf{E}_i \dot{\boldsymbol{\phi}}). \tag{5}$$

Assuming quasistatic motion, the swimmer is in static equilibrium $\mathbf{F}_b = 0$. Using (5), the dynamic equations of swimming, which are a linear relation between the swimmer's shape velocity $\dot{\boldsymbol{\phi}}$ and body velocity $\dot{\mathbf{q}}$, are obtained as

$$\dot{\mathbf{q}} = \boldsymbol{\mathcal{G}}(\mathbf{q}, \boldsymbol{\phi})\dot{\boldsymbol{\phi}}, \quad \text{where} \tag{6}$$

$$\boldsymbol{\mathcal{G}}(\mathbf{q}, \boldsymbol{\phi}) = -\left(\textstyle\sum_{i=0}^{2} \mathbf{T}_i^T \boldsymbol{\mathcal{R}}_i \mathbf{T}_i\right)^{-1} \left(\textstyle\sum_{i=0}^{2} \mathbf{T}_i^T \boldsymbol{\mathcal{R}}_i \mathbf{E}_i\right).$$

From the expressions for $\mathbf{T}_i$ and $\boldsymbol{\mathcal{R}}_i$ in (2) and (4), it is clear that the square matrix in (6) is symmetric and positive definite, and hence invertible. This is in contrast to locomotion systems based on kinematic constraints where singular configurations are possible, as in the kinematic snake model [31].

III. Symmetries of Velocity and Finite Motion

In this section, symmetries of the swimmer's motion are analyzed. We begin with formulating symmetries of the velocity relation (6), which were already analyzed in [25]. Then we define reflection operators on trajectories of shape change and formulate symmetries of finite body motion.

A. Velocity symmetries ([25])

The first symmetry is called *gauge symmetry* [15]. It represent the fact that in an unbounded fluid domain, the relation (6) is invariant under rigid body motion of $\mathbf{q}$ [1], [2], [5].

1) Gauge symmetry: The matrix $\boldsymbol{\mathcal{G}}(\mathbf{q}, \boldsymbol{\phi})$ in (6) can be decomposed into:

$$\boldsymbol{\mathcal{G}}(\mathbf{q}, \boldsymbol{\phi}) = \mathbf{D}(\theta)\mathbf{G}(\boldsymbol{\phi}),$$

$$\text{where } \mathbf{D}(\theta) = \begin{bmatrix} \cos\theta & -\sin\theta & 0 \\ \sin\theta & \cos\theta & 0 \\ 0 & 0 & 1 \end{bmatrix} \tag{7}$$

This special structure is due to the fact that the body velocity expressed in body-fixed reference frame depends only on the shape variables $\boldsymbol{\phi}$ and their velocities $\dot{\boldsymbol{\phi}}$. The matrix $\mathbf{G}(\boldsymbol{\phi})$ in (7) is precisely the *principal connection* of the swimmer's motion [1], [2], [26]. The next two symmetries are of different nature, since they are related to additional structure of $\mathbf{G}(\boldsymbol{\phi})$ due to geometric symmetries of the three-link swimmer.

2) Axial Symmetry: This symmetry is due to the fact that the swimmer possesses symmetry about the longitudinal axis of the middle link, see Fig. 2(a). This is expressed by the relation:

$$\mathbf{G}(-\boldsymbol{\phi}) = \begin{bmatrix} -1 & 0 & 0 \\ 0 & 1 & 0 \\ 0 & 0 & 1 \end{bmatrix} \mathbf{G}(\boldsymbol{\phi}) \triangleq f_1(\mathbf{G}(\boldsymbol{\phi})) \tag{8}$$

(a) (b)

Fig. 2: Velocity Symmetries: (a) Axial Symmetry - influence of reversing the joint angles ϕ_i on body velocity $\dot{\mathbf{q}}$. (b) Front-Back symmetry - influence of swapping the joint angles ϕ_i and their velocities $\dot{\phi}_i$ on body velocity $\dot{\mathbf{q}}$.

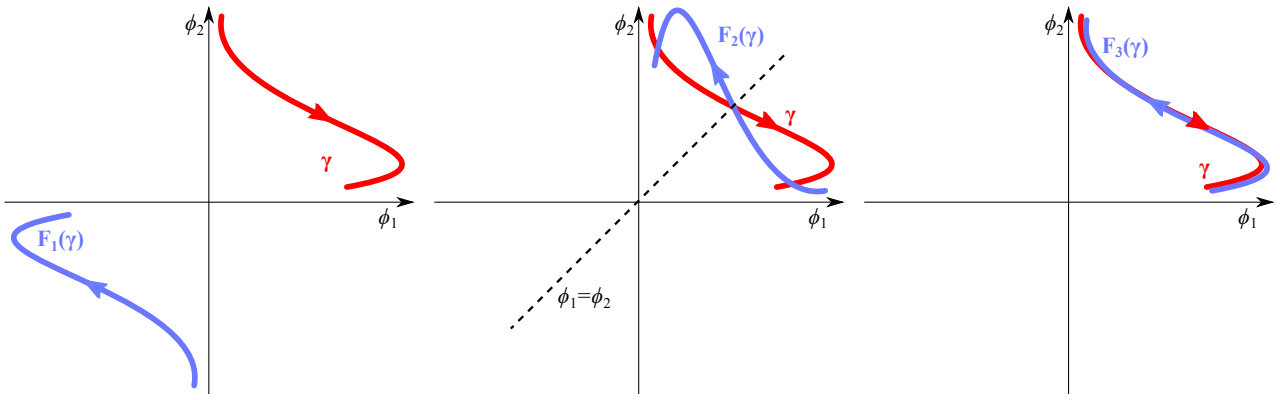

(a) (b) (c)

Fig. 3: Reflections of shape trajectories: (a) Axial reflection F_1 - the trajectory $F_1(\gamma)$ is obtained by reversing the sign of $\phi_i(t)$. (b) Front-back reflection F_2 - the trajectory $F_2(\gamma)$ is obtained by swapping the angles $\phi_1(t)$ and $\phi_2(t)$. (c) Time reversal reflection F_3 - the trajectory $F_3(\gamma)$ obtained by time reversal of the motion along γ.

3) Front-Back Symmetry: This symmetry stems from the fact that the swimmer's two distal links are identical, i.e. l_1=l_2, hence the swimmer possesses symmetry about the bisecting line of the middle link, see Fig. 2(b). This relation can be expressed as:

$$\mathbf{G}(\mathbf{S}\boldsymbol{\phi}) = \begin{bmatrix} -1 & 0 & 0 \\ 0 & 1 & 0 \\ 0 & 0 & -1 \end{bmatrix} \mathbf{G}(\boldsymbol{\phi})\mathbf{S} \triangleq f_2(\mathbf{G}(\boldsymbol{\phi})) \tag{9}$$

where $\mathbf{S} = \begin{bmatrix} 0 & 1 \\ 1 & 0 \end{bmatrix}$.

The matrix $\mathbf{S}$ in (9) represents swapping between the front and back links 1 and 2.

B. Finite Rigid-Body Motion and Finite Shape Changes

Unlike velocity relations which correspond to *infinitesimal* motions, integration of rigid-body and shape velocities along a *finite* time requires treatment of net body motion. Therefore, we now define the homogenous matrix representation of rigid body motion, and the notation of shape trajectory. A body position $\mathbf{q} = (x, y, \theta)^T$ can be represented by the homogeneous rigid-body transformation matrix as:

$$\mathbf{A}(\mathbf{q}) = \begin{bmatrix} \cos\theta & -\sin\theta & x \\ \sin\theta & \cos\theta & y \\ 0 & 0 & 1 \end{bmatrix}. \tag{10}$$

A trajectory γ of shape changes is a time-parametrized change of the joint angles $\gamma = \boldsymbol{\phi}(t) = (\phi_1(t), \phi_2(t))^T$ for $t \in [0, T]$. The net body motion $\mathbf{q}(T)$ under initial conditions $\mathbf{q}(0)$=$\mathbf{q}_0$=$(x_0, y_0, \theta_0)^T$ and shape changes along the trajectory γ is obtained by integrating the dynamic equation (6) in time, and is denoted by $\boldsymbol{\psi}(\gamma, \mathbf{q}_0)$. The following proposition reviews a key result [1], [5], [15] which extends the gauge symmetry property from velocity level (7) into finite motions generated by shape trajectories. It states that any shape trajectory generates a particular net body motion relative to the starting body frame. (This concept is often called the *geometric phase* of a gait [1]).

Proposition 1 ([1], [5], [15])**.** *The net body motion under initial conditions* $\mathbf{q}_0$ *and a given shape trajectory* γ *satisfies*

$$\mathbf{A}(\boldsymbol{\psi}(\gamma, \mathbf{q}_0)) = \mathbf{A}(\mathbf{q}_0)\mathbf{A}(\boldsymbol{\psi}(\gamma, 0)). \tag{11}$$

The proof of the proposition appears in the Appendix. Using this proposition, we can define: $\mathbf{A}_\gamma = \mathbf{A}(\boldsymbol{\psi}(\gamma, 0))$ which is a transformation matrix that represents the swimmer's position after applying the shape trajectory γ under zero initial conditions $\mathbf{q}(0)$=0. Note that $\mathbf{A}_\gamma$ is independent of time parametrization of the motion along the shape trajectory γ, due to the time-invariance of (6).

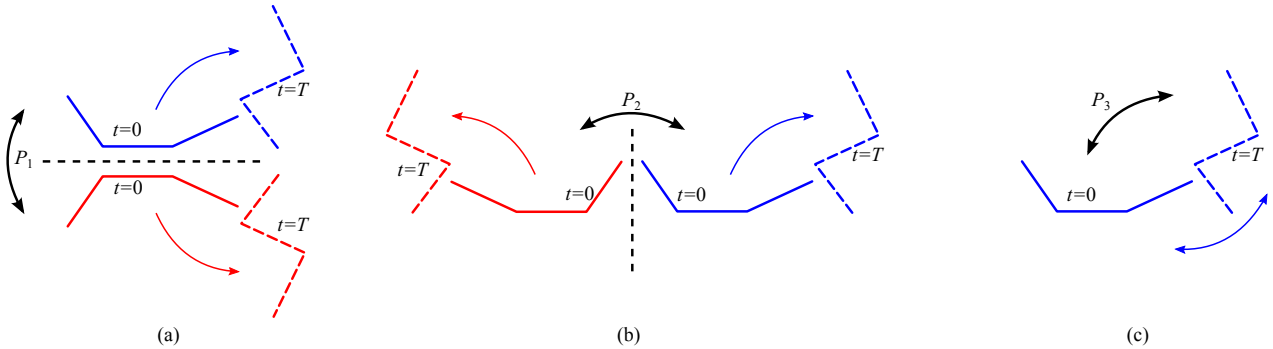

Fig. 4: Symmetries of Finite Motion: (a) P_1 - change in net body motion under applying the axial reflection F_1 to γ. (b) P_2 - change in net body motion under applying the front-back reflection F_2 to γ. (c) P_3 - change in net body motion under applying the time reversal reflection F_3 to γ.

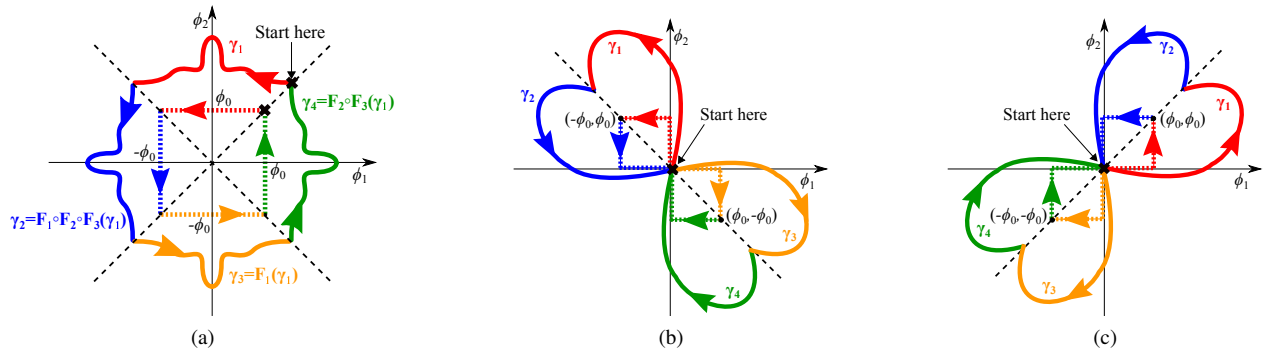

Fig. 5: Three types of symmetric gaits: (a) Gait 1 (Square Gait of Purcell in dashed lines) - the net motion is in x direction. (b) Gait 2 (rectilinear loop in dashed lines) - the net motion is in y direction. (c) Gait 3 (rectilinear loop in dashed lines) - the net motion is almost pure rotation.

C. Shape Trajectory Reflections

We now define three different reflection operators on shape trajectories. These operators are necessary for extending the velocity symmetries listed above to symmetries of finite rigid-body motion of the swimmer. Consider a given shape trajectory γ and its time parametrization $\boldsymbol{\phi}(t)$ for $t \in [0, T]$. The operator of axial reflection F_1, which corresponds to sign reversal of the joint angles, is defined as:

$$F_1(\boldsymbol{\phi}(t)) = -\boldsymbol{\phi}(t) \tag{12}$$

The operator of front-back reflection F_2, which corresponds to swapping of the two joint angles, is defined as:

$$F_2(\boldsymbol{\phi}(t)) = \mathbf{S}\boldsymbol{\phi}(t) \tag{13}$$

where $\mathbf{S}$ is the swap matrix defined in (9). Finally, the operator of time reversal F_3 is defined as:

$$F_3(\boldsymbol{\phi}(t)) = \boldsymbol{\phi}(T - t). \tag{14}$$

A graphical representation of the three reflection operators' action on shape trajectories γ in ϕ_1–ϕ_2 plane is shown in Fig. 3.

D. Symmetries of Finite Motion

We now use the reflection operators defined above in order to formulate the symmetries of finite motions of the swimmer. Consider a given shape trajectory γ and its time parametrization $\boldsymbol{\phi}(t)$. The net rigid body motion under the action of the shape change γ and zero initial conditions $\mathbf{q}(0) = 0$ is denoted by $\boldsymbol{\psi}(\gamma, 0) = (x, y, \theta)^T$. The following three theorems summarize the inherited symmetries of finite rigid-body motions obtained by time-integration along symmetry-reflected shape trajectories by formulating the change in net motion due to application of each of the three reflection operators on the shape trajectory γ:

Theorem 1. *Under the axial reflection operator F_1, one obtains:*

$$\mathbf{A}_{F_1(\gamma)} = \begin{bmatrix} \cos\theta & \sin\theta & x \\ -\sin\theta & \cos\theta & -y \\ 0 & 0 & 1 \end{bmatrix} \triangleq P_1(\mathbf{A}_\gamma). \tag{15}$$

Theorem 2. *Under the front-back reflection operator F_2, one obtains:*

$$\mathbf{A}_{F_2(\gamma)} = \begin{bmatrix} \cos\theta & \sin\theta & -x \\ -\sin\theta & \cos\theta & y \\ 0 & 0 & 1 \end{bmatrix} \triangleq P_2(\mathbf{A}_\gamma). \tag{16}$$

Theorem 3. *Under the time-reversal reflection operator F_3, one obtains:*

$$\mathbf{A}_{F_3(\gamma)} = \mathbf{A}_\gamma^{-1} = \begin{bmatrix} \cos\theta & \sin\theta & -x\cos\theta - y\sin\theta \\ -\sin\theta & \cos\theta & x\sin\theta - y\cos\theta \\ 0 & 0 & 1 \end{bmatrix} \triangleq P_3(\mathbf{A}_\gamma) \tag{17}$$

Note that this theorem is strongly related to Purcell's classical *scallop theorem* [17], which stated that under a reciprocal shape trajectory, the rigid-body motion cancels itself and results in zero net motion.

The proofs of the theorems 1, 2 and 3 appear in the Appendix. A graphical representation of the three symmetry operators of finite rigid-body motion is shown in Fig. 4.

IV. Symmetric Gaits

In this section we propose three types of symmetric gaits, and analyze the resulting net rigid-body motion of the swimmer. A gait is defined as a shape trajectory γ that forms a closed curve, and thus it can be applied repeatedly as a time-periodic input. Each of the three gait types is decomposed into a concatenation of four sub-paths γ_1 to γ_4 which are connected at their endpoints according to $\gamma_{\underline{i+1}}(0) = \gamma_i(T)$ for i=1 . . . 4, where $\underline{i} = \{i \mod 4\}$. Each of the three gait types satisfies certain symmetries, so that its four sub-paths γ_i are interrelated via reflection operators. This, in turn, affects the net body motion under each of the three gaits, as detailed below. Typical gaits from each type are shown in Fig. 5, where the closed loops of dashed lines are representative rectilinear gaits with angular amplitude of ϕ_0.

A. Gait 1

Gait type 1 possesses two axes of symmetry along the lines ϕ_1=ϕ_2 and ϕ_1= − ϕ_2 in $\phi_1 - \phi_2$ plane, as shown in Fig. 5(a), where the natural representative is Purcell's square gait from Fig. 1(b). Using the symmetries defined in the previous section, it is now easy to prove Purcell's statement that this type of symmetric gait results in motion along x direction only. The four sub-paths of this gait satisfy the relations:

$$\begin{aligned}\gamma_2 &= F_1 \circ F_2 \circ F_3(\gamma_1)\\ \gamma_3 &= F_1(\gamma_1)\\ \gamma_4 &= F_2 \circ F_3(\gamma_1)\end{aligned} \tag{18}$$

Note that the endpoints of γ_1 satisfy $\phi_1(0)$=$\phi_2(0)$ and $\phi_1(T)$= − $\phi_2(T)$. Denoting the net rigid-body motion under the sub-path γ_1 as $\boldsymbol{\psi}(\gamma_1, 0) = (x, y, \theta)^T$, one can obtain the motion under each of the other sub-paths γ_2 to γ_4 by using the symmetry theorems 1-3, as:

$$\mathbf{A}_{\gamma_1} = \begin{bmatrix} \cos\theta & -\sin\theta & x \\ \sin\theta & \cos\theta & y \\ 0 & 0 & 1 \end{bmatrix}$$

$$\mathbf{A}_{\gamma_2} = P_1(P_2(P_3(\mathbf{A}_{\gamma_1}))) = \begin{bmatrix} \cos\theta & \sin\theta & x\cos\theta + y\sin\theta \\ -\sin\theta & \cos\theta & -x\sin\theta + y\cos\theta \\ 0 & 0 & 1 \end{bmatrix}$$

$$\mathbf{A}_{\gamma_3} = P_1(\mathbf{A}_{\gamma_1}) = \begin{bmatrix} \cos\theta & \sin\theta & x \\ -\sin\theta & \cos\theta & -y \\ 0 & 0 & 1 \end{bmatrix}$$

$$\mathbf{A}_{\gamma_4} = P_2(P_3(\mathbf{A}_{\gamma_1})) = \begin{bmatrix} \cos\theta & -\sin\theta & x\cos\theta + y\sin\theta \\ \sin\theta & \cos\theta & x\sin\theta - y\cos\theta \\ 0 & 0 & 1 \end{bmatrix}$$

Finally, in order to obtain the net rigid-body motion under the entire gait γ, one has to invoke Proposition 1 and simply multiply the four transformation matrices $\mathbf{A}_{\gamma_i}$, which yields:

$$\mathbf{A}_{\gamma} = \mathbf{A}_{\gamma_1}\mathbf{A}_{\gamma_2}\mathbf{A}_{\gamma_3}\mathbf{A}_{\gamma_4} = \begin{bmatrix} 1 & 0 & 4x \\ 0 & 1 & 0 \\ 0 & 0 & 1 \end{bmatrix} \tag{19}$$

We can see that the resulting net motion is only along x direction without rotation, since the net-body motions of the four sub-paths in directions of y and θ are cancelled while the motion along x is summed.

B. Gait 2

The second gait type possesses symmetries of a figure-eight shape (Fig. 5(b)), and results in net motion along y direction, as proven below. The four sub-paths of the gait are related by the following reflection operators:

$$\begin{aligned}\gamma_2 &= F_1 \circ F_2 \circ F_3(\gamma_1)\\ \gamma_3 &= F_2(\gamma_1)\\ \gamma_4 &= F_1 \circ F_3(\gamma_1)\end{aligned} \tag{20}$$

Note that the endpoints of γ_1 satisfy $\phi_1(0)$=$\phi_2(0)$=0 and $\phi_1(T)$= − $\phi_2(T)$. Using the symmetry theorems 1-3, the net rigid-body motions under each sub-path are given by:

$$\mathbf{A}_{\gamma_1} = \begin{bmatrix} \cos\theta & -\sin\theta & x \\ \sin\theta & \cos\theta & y \\ 0 & 0 & 1 \end{bmatrix}$$

$$\mathbf{A}_{\gamma_2} = P_1(P_2(P_3(\mathbf{A}_{\gamma_1})))$$

$$\mathbf{A}_{\gamma_3} = P_2(\mathbf{A}_{\gamma_1})$$

$$\mathbf{A}_{\gamma_4} = P_1(P_3(\mathbf{A}_{\gamma_1})).$$

Finally, in order to obtain the net rigid-body motion under the entire gait γ, one has to multiply the four transformation matrices $\mathbf{A}_{\gamma_i}$, which yields:

$$\mathbf{A}_{\gamma} = \mathbf{A}_{\gamma_1}\mathbf{A}_{\gamma_2}\mathbf{A}_{\gamma_3}\mathbf{A}_{\gamma_4} = \begin{bmatrix} 1 & 0 & 0 \\ 0 & 1 & 4y \\ 0 & 0 & 1 \end{bmatrix} \tag{21}$$

One can see that the net motion is only along y direction, while the motions along x and θ are canceled.

C. Gait 3

The third gait type possesses symmetries of a different figure-eight shape, as shown in Fig. 5(c). The four sub-paths of this gait satisfy the relations:

$$\begin{aligned}\gamma_2 &= F_2 \circ F_3(\gamma_1)\\ \gamma_3 &= F_1 \circ F_2(\gamma_1)\\ \gamma_4 &= F_1 \circ F_3(\gamma_1)\end{aligned} \tag{22}$$

Note that the endpoints of γ_1 satisfy $\phi_1(0)$=$\phi_2(0)$=0 and $\phi_1(T)$=$\phi_2(T)$. Using the symmetry theorems 1-3, the net rigid-body motions under each sub-path are given by:

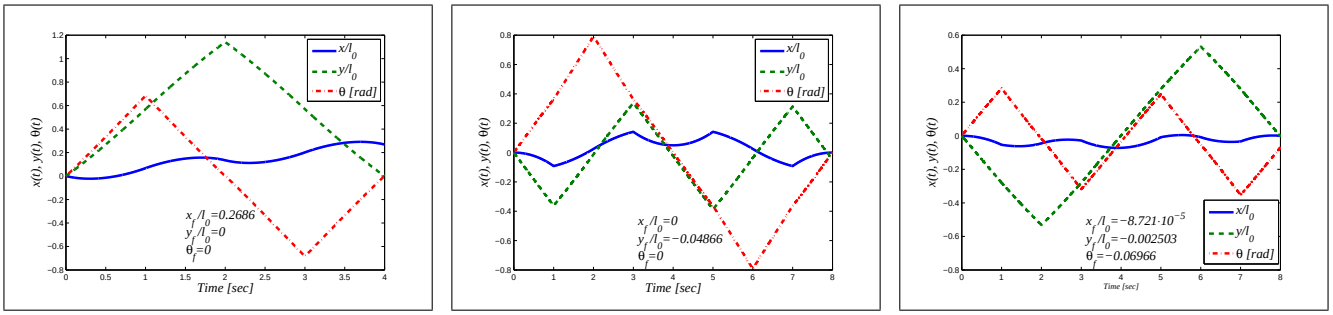

(a) (b) (c)

Fig. 6: Simulation results (l_0=8.4, l_1=l_2=14): (a) Square gait 1: $\phi_0 = 55°$. The net body motion is only in x direction; (b) Rectilinear gait 2: $\phi_0 = 65°$. The net body motion is only in y direction. c. Rectilinear gait 3: $\phi_0 = 50°$. The net body motion is almost pure rotation.

$$\mathbf{A}_{\gamma_1} = \begin{bmatrix} \cos\theta & -\sin\theta & x \\ \sin\theta & \cos\theta & y \\ 0 & 0 & 1 \end{bmatrix}$$
$$\mathbf{A}_{\gamma_2} = P_2(P_3(\mathbf{A}_{\gamma_1}))$$
$$\mathbf{A}_{\gamma_3} = P_1(P_2(\mathbf{A}_{\gamma_1}))$$
$$\mathbf{A}_{\gamma_4} = P_1(P_3(\mathbf{A}_{\gamma_1}))$$

Finally, in order to obtain the net rigid-body motion under the entire gait γ, one has to multiply the four transformation matrices $\mathbf{A}_{\gamma_i}$, which yields:

$$\mathbf{A}_\gamma = \mathbf{A}_{\gamma_1}\mathbf{A}_{\gamma_2}\mathbf{A}_{\gamma_3}\mathbf{A}_{\gamma_4} = \quad (23)$$
$$\begin{bmatrix} \cos 4\theta & -\sin 4\theta & x(1-\cos 4\theta) + y(2\sin 2\theta - \sin 4\theta) \\ \sin 4\theta & \cos 4\theta & -x\sin 4\theta + y(1 - 2\cos 2\theta + \cos 4\theta) \\ 0 & 0 & 1 \end{bmatrix}$$

One can see that the rotations under each sub-path γ_i are summed, but the net translation along x and y directions is not exactly cancelled. Nevertheless, if the rotation θ is small, the net translation becomes negligible. This is demonstrated in the numerical simulations below. Note that gaits that generate pure rotation with exact cancellation of the translation are not possible to obtain via symmetry principles only. Nevertheless, asymmetric gaits that achieve this can be obtained numerically via trial and error.

Effect of changing the starting point: In the three gaits given above, it is clear that the choice of a starting point is of crucial importance. For each gait, the starting point was chosen to lie on one of the symmetry axes (i.e. ϕ_1=ϕ_2 and ϕ_1=$-\phi_2$) or their intersection point, in order to achieve the desired cancellations and generate net motion along a principal direction. The effect of changing the starting point of a gait is explained as follows (cf. [1], [2], [5]). Let Γ denote a closed shape trajectory with a starting point p, and let Γ' be a gait with the same trajectory and a different starting point q. Using Proposition 1 and Theorem 3, the influence of changing the starting point on the net body motion represented by homogeneous rigid-body transformation matrices is given by the relation: $\mathbf{A}_{\Gamma'} = \mathbf{A}_\gamma \mathbf{A}_\Gamma \mathbf{A}_\gamma^{-1}$, where γ is the sub-path from q to p, as illustrated in Fig. 7. Due to the structure of transformation matrices of $SE(2)$ as in (10), it is clear that the net rotation is not affected by the choice of a starting point. On the other hand, the net translation is affected by this change due to non-commutativity of translations and rotations in $SE(2)$. For gaits that result in zero net rotation such as gaits 1 and 2 (and 4,5 in Section VI), the net translation is simply rotated from one body-fixed frame to another.

D. Simulation Results

We now demonstrate the motion of Purcell's swimmer under each of the three gait types. The values of the links' length are chosen as $l_0 = 8.4\ cm, l_1 = l_2 = 14\ cm$, and their cross-section radius is a=0.25 cm, which correspond to the physical lengths of the robotic prototype presented in Section VII. The chosen gaits are the rectilinear loops shown in dashed lines in Fig. 5. The angular amplitudes ϕ_0 of gaits $\{1, 2, 3\}$ are chosen as $\{55°,\ 65°,\ 50°\}$ respectively, again in accordance with the experiments. The gaits period times T were chosen as $\{4, 8, 8\}$ seconds. Fig. 6a,b,c show time plots of the body position $x(t), y(t)$ normalized by the middle link length l_0 and the body orientation $\theta(t)$ in radians. For each gait, the final values (x_f, y_f, θ_f) at time t=T appear in the text on the plots. Multimedia movie files animating the swimmer's motion

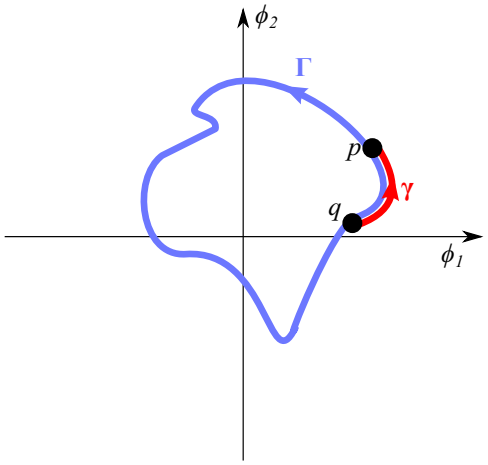

Fig. 7: Illustration of changing the starting point of a gait.

under these three gaits can be found in the supplementary material. The simulation results indicate that the motion in x direction under gait 1 is significantly larger than the motion in y direction under gait 2, and that the net translation under gait 3 is significantly smaller than the net rotation. These observations are formally justified in the next section which studies scaling of the motion under small-amplitude gaits.

V. Scaling of motion under small-amplitude gaits

In this section, the scaling of net body motion under small-amplitude symmetric gaits is formulated. Assume that a trajectory γ is of small amplitude of joint angles about the straightened configuration $\boldsymbol{\phi}$=0. Let the shape trajectory γ be described by a small scaling parameter $\varepsilon \ll 1$ of amplitude, such that γ=$\varepsilon\boldsymbol{\phi}(t)$ where $\boldsymbol{\phi}(t) = O(1)$. For example, one can think of the stroke amplitude ϕ_0 of the rectilinear dashed loops in Fig. 5 as a representative of ε. Using this representation of a given gait, one can find the scaling of the resulting net body motion by using perturbation expansion [35] of the equation of motion (6). This is summarized in the following theorem.

Theorem 4. *Consider Purcell's three-link swimmer under a small-amplitude gait γ=$\varepsilon\boldsymbol{\phi}(t)$, where $\varepsilon \ll 1$. Let $\mathbf{q}_f = (x_f, y_f, \theta_f)$ be the net body motion under the given gait and $\mathbf{q}(0)$=0. Then for a symmetric gait of type 1, x_f scales as ε^2, and for a symmetric gait of type 2, y_f scales as ε^3. For a symmetric gait of type 3, the net rotation θ_f scales as ε^3, the translation y_f scales as ε^5, and x_f scales as ε^8. These results are summarized in table I.*

Gait	x_f	y_f	θ_f
1	ε^2	0	0
2	0	ε^3	0
3	ε^8	ε^5	ε^3

TABLE I: Scaling of net motion under $O(\varepsilon)$ gaits

The proof of Theorem 4 appears in the Appendix. It involves expanding $\mathbf{G}(\boldsymbol{\phi})$ from (7) as a Taylor series in ϕ_1 and ϕ_2. Then, the equation of motion (6) is integrated along the given trajectory in two stages – leading-order expression for the rotation $\theta(t)$ are obtained first, followed by expressions for $x(t)$ and $y(t)$, while accounting for cancellations due to symmetries of the particular gait. While the scaling of $x_f = O(\varepsilon^2)$ for gait type 1 is already known and has been obtained in different ways in [24], [36], [37], the results on gaits 2 and 3 are an original contribution of this work. This also corroborates the large differences in x_f,y_f and θ_f in the numerical simulations under the three different rectilinear gaits as shown in Fig. 6.

VI. Gaits for swimmers with one symmetry axis

In this section we analyze three-link swimmer models with only one axis of symmetry, which are much more realistic and biologically relevant. Fig. 8(a) shows a swimmer with axial symmetry and no front-back symmetry. This model is reminiscent of a typical sperm cell with a spherical head and thin elongated tail [7], [22]. Fig. 8(c) shows a swimmer with front-back symmetry and no axial symmetry. This structure of a big spherical cell at the middle connected to two identical thin "arms" is reminiscent of the alga *Chlamydomonas* [7], [38].

The equations of motion for these swimmer models are formulated using a straightforward extension of the derivation in Section II, as follows. The sphere is incorporated into the formulation in (6) as an additional link with i=3, whose matrices $\mathbf{T}_3$ and $\mathbf{E}_3$ in the kinematic relation (1) are easily constructed. Neglecting hydrodynamic interaction between the sphere and the slender links, the resistance tensor of the sphere is known (cf. [12]), and is given by

$$\boldsymbol{\mathcal{R}}_3 = 2\pi\mu r \begin{bmatrix} 3 & 0 & 0 \\ 0 & 3 & 0 \\ 0 & 0 & 4r^2 \end{bmatrix}$$

where r is the radius of the sphere and μ is the fluid's viscosity. Then, the equation of motion (6) holds while $\boldsymbol{\mathcal{G}}(\mathbf{q}, \boldsymbol{\phi})$ is computed under summation of i=0 . . . 3.

In order to generate net translation in a desired direction for these swimmers while the net rotation is cancelled, additional symmetric gaits are proposed and analyzed, which exploit only the remaining structural symmetries.

A. Swimmer with axial symmetry — Gait 4

A three-link swimmer with axial symmetry and broken front-back symmetry is depicted in Fig. 8(a). This type of swimmer possesses the axial symmetry P_1 of body motion from equation (15) while the front-back symmetry P_2 from equation (16) does not hold. The proposed symmetric gait for this swimmer, denoted as gait 4, is shown in Fig. 8(b). This gait consists of two concatenated sub-paths γ_1 and γ_2 that are related by the axial reflection operator, such that $\gamma_2 = F_1(\gamma_1)$. This gait does not make use of the front-back reflection F_2 due to loss of the corresponding symmetry in the swimmer's structure. Let (x, y, θ) denote the swimmer's motion under the shape trajectory γ_1 and $\mathbf{q}(0) = 0$. Using Theorem 1, the matrix representation of net rigid-body motion under γ_1 and γ_2 are related according to:

$$\mathbf{A}_{\gamma_1} = \begin{bmatrix} \cos\theta & -\sin\theta & x \\ \sin\theta & \cos\theta & y \\ 0 & 0 & 1 \end{bmatrix}$$

$$\mathbf{A}_{\gamma_2} = P_1(\mathbf{A}_{\gamma_1}) = \begin{bmatrix} \cos\theta & \sin\theta & x \\ -\sin\theta & \cos\theta & -y \\ 0 & 0 & 1 \end{bmatrix}$$

The net rigid-body motion under the entire gait γ is obtained by matrix multiplication as

$$\mathbf{A}_{\gamma} = \mathbf{A}_{\gamma_1}\mathbf{A}_{\gamma_2} = \begin{bmatrix} 1 & 0 & x(1+\cos\theta) + y\sin\theta \\ 0 & 1 & y(1-\cos\theta) + x\sin\theta \\ 0 & 0 & 1 \end{bmatrix}. \quad (24)$$

It can be seen that gait 4 results in pure translation while the net rotation is cancelled. Moreover, for small rotation θ, the motion in x direction is much larger than the motion in y direction. For a small-amplitude gait γ=$\varepsilon\boldsymbol{\phi}(t)$, scaling of the net motion is summarized in the following theorem.

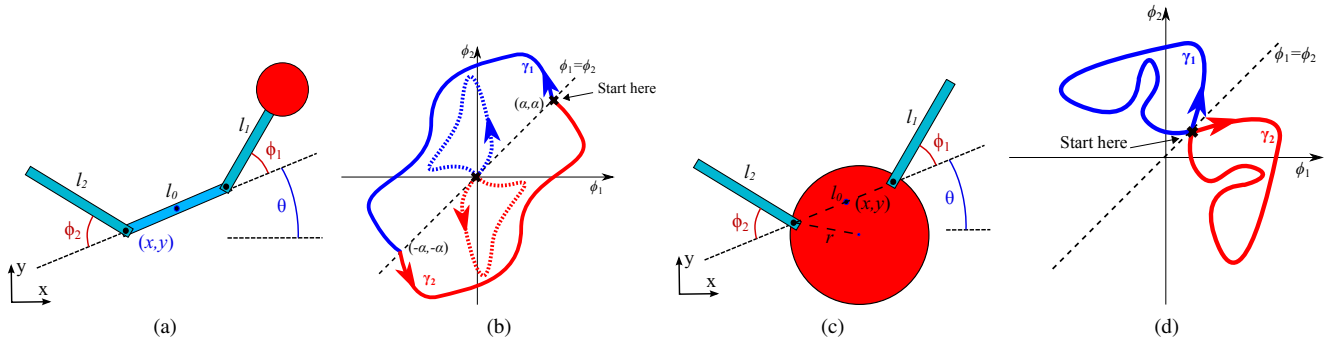

Fig. 8: Swimmers with a single axis of symmetry and their Gaits: (a) Sperm-like swimmer with axial symmetry and no front-back symmetry. (b) Gait 4 whose two sub-paths satisfy $\gamma_2{=}F_1(\gamma_1)$. (c) A swimmer with right-left symmetry and no axial symmetry. (d) Gait 5 whose two sub-paths satisfy $\gamma_2{=}F_2(\gamma_1)$.

Theorem 5. *Consider the three-link swimmer with axial symmetry under the symmetric gait 4 with small amplitude* $\gamma{=}\varepsilon\boldsymbol{\Phi}(t)$*, where* $\varepsilon \ll 1$*. Let* $\mathbf{q}_f = (x_f, y_f, \theta_f)$ *be the net body motion for* $\mathbf{q}(0){=}0$*. Then the net rotation* θ_f *is zero,* x_f *scales as* ε^2*, and* y_f *scales as* ε^3*. Moreover, if the gait also satisfies* $\boldsymbol{\Phi}(0){=}0$ *then* y_f *is even smaller and scales as* ε^5 *while* $x_f{=}O(\varepsilon^2)$*.*

The proof of this theorem appears in the Appendix.

B. Swimmer with front-back symmetry — Gait 5

A three-link swimmer with front-back symmetry and broken axial symmetry is depicted in Fig. 8(c). This type of swimmer possesses the front-back symmetry P_2 of body motion from equation (16) while the axial symmetry P_1 from equation (15) does not hold. The proposed symmetric gait for this swimmer, denoted as gait 5, is shown in Fig. 8(d). This gait consists of two concatenated sub-paths γ_1 and γ_2 that are related by the front-back reflection operator, such that $\gamma_2 = F_2(\gamma_1)$. This gait does not make use of the axial reflection F_1 due to loss of the corresponding symmetry in the swimmer's structure. Let (x, y, θ) denote the swimmer's motion under the shape trajectory γ_1 and $\mathbf{q}(0) = 0$. Using Theorem 2, the matrix representation of net rigid-body motion under γ_1 and γ_2 are related according to:

$$\mathbf{A}_{\gamma_1} = \begin{bmatrix} \cos\theta & -\sin\theta & x \\ \sin\theta & \cos\theta & y \\ 0 & 0 & 1 \end{bmatrix}$$

$$\mathbf{A}_{\gamma_2} = P_2(\mathbf{A}_{\gamma_1}) = \begin{bmatrix} \cos\theta & \sin\theta & -x \\ -\sin\theta & \cos\theta & y \\ 0 & 0 & 1 \end{bmatrix}$$

The net rigid-body motion under the entire gait γ is obtained by matrix multiplication as

$$\mathbf{A}_{\gamma} = \mathbf{A}_{\gamma_1}\mathbf{A}_{\gamma_2} = \begin{bmatrix} 1 & 0 & x(1-\cos\theta) - y\sin\theta \\ 0 & 1 & y(1+\cos\theta) - x\sin\theta \\ 0 & 0 & 1 \end{bmatrix} \quad (25)$$

It can be seen that gait 5 results in pure translation while the net rotation is cancelled. Moreover, for small rotation θ, the motion in y direction is much larger than the motion in x direction. For a small-amplitude gait $\gamma{=}\varepsilon\boldsymbol{\Phi}(t)$, scaling of the net motion is summarized in the following theorem.

Theorem 6. *Consider the three-link swimmer with front-back symmetry under the symmetric gait 5 with small amplitude* $\gamma{=}\varepsilon\boldsymbol{\Phi}(t)$*, where* $\varepsilon \ll 1$*. Let* $\mathbf{q}_f = (x_f, y_f, \theta_f)$ *be the net body motion for* $\mathbf{q}(0){=}0$*. Then the net rotation* θ_f *is zero,* y_f *scales as* ε^3*, and* x_f *scales as* ε^5*.*

The proof of this theorem appears in the Appendix.

C. Simulation Results

We now show numerical simulation results of these two types of swimmers. The first simulation is that of the sperm-like swimmer shown in Fig. 8(a) with links lengths $l_0 = 8.4\ cm$, $l_1 = l_2 = 14\ cm$ and head radius of $r{=}2.1\ cm$. The chosen symmetric gait of type 4 is the skewed figure-eight loop shown in Fig. 9(a), with stroke amplitude $\phi_0{=}60°$. Time plots of the body position $x(t), y(t)$ normalized by the middle link length l_0 and the body orientation $\theta(t)$ in radians are shown in Fig. 9(b). The final values (x_f, y_f, θ_f) at time $t{=}T$ appear in the text on the plot. The second simulation is that of the swimmer model shown in Fig. 8(c) with the same links lengths, where the middle link is replaced by a sphere of radius $r{=}5.94\ cm$. The chosen symmetric gait of type 5 is the triangular loop shown in Fig. 9(c), with stroke amplitude $\phi_0{=}80°$. Time plots of $x(t)$, $y(t)$ and $\theta(t)$ are shown in Fig. 9(d), while the final values (x_f, y_f, θ_f) appear in the text on the plot. The large differences in both x_f and y_f in the results of the simulations under the two gaits are in agreement with the scaling analysis in Theorems 5 and 6.

Animation movies of the simulated motion under gaits 4 and 5 can be found in the supplementary material. It can be seen that the motion of the axially-symmetric swimmer under gait 4 is similar to the motion of a sperm cell which moves forward towards its head, while the motion of the links resembles a travelling wave along the tail. Moreover, the symmetries of gait 4 imply that the undulation amplitude of the wave can increase or decrease from head to tail, an effect which has actually been observed in motion of sperms [39]. On the other hand, the motion of the right-left (front-back) symmetric swimmer under gait 5 is substantially different from the typical motion

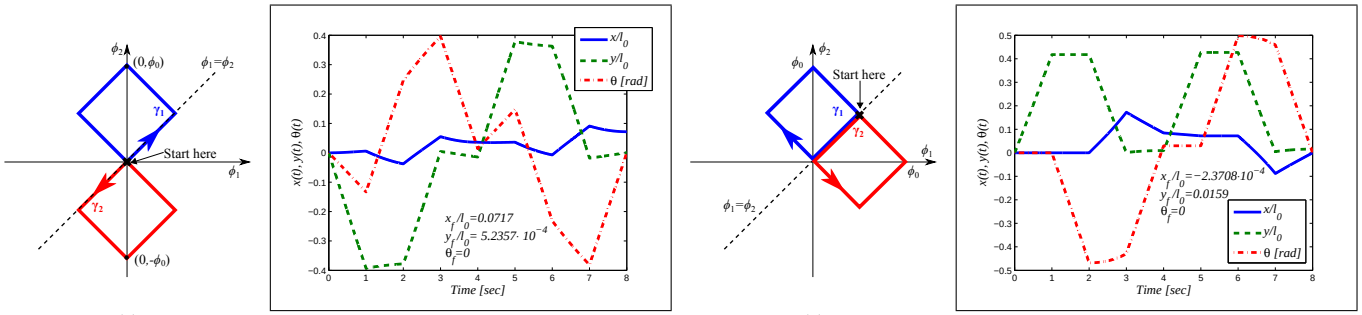

(a) (b) (c) (d)

Fig. 9: Numerical simulation results of gaits 4 and 5: (a) Skewed figure-eight loop of gait 4 for the sperm-like swimmer. (b) Simulation results under gait 4 with stroke amplitude ϕ_0=60°. The net body motion is pure translation almost along x direction. (c) Triangular figure-eight loop gait 5 for the right-left symmetric swimmer. (d) Simulation results under gait 5 with stroke amplitude ϕ_0=80°. The net body motion is pure translation almost along y direction.

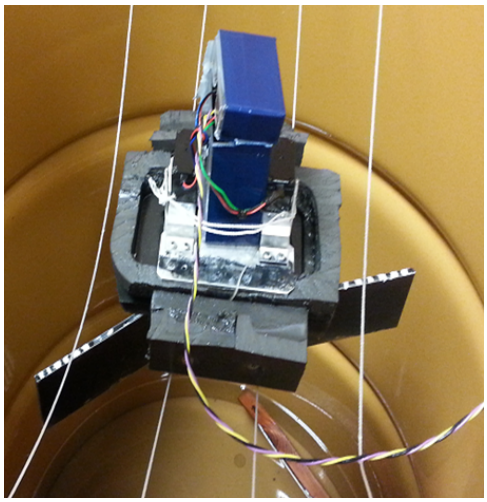

Fig. 10: The experimental macro-scale robotic prototype of Purcell's three link swimmer.

observed in *Chlamydomonas* swimming [38]. One reason for this difference is the fact that the two flagella of the alga are deformable and thus they can perform strokes which are identical up to right-left reflection but break time-reversibility and thus enable efficient propulsion along y direction only. In our model where the two "arms" are rigid links, any right-left symmetric stroke (i.e. $\phi_1(t)$=$\phi_2(t)$) is a reciprocal motion that does not generate net propulsion.

VII. Robotic Macro-Swimmer Experiments

In this section, motion experiments with a macro-robotic swimmer prototype are presented. The swimmer prototype, shown in Fig. 10, consists of three thin aluminum plates that represent the links. The thickness of the plates is $2a = 0.5\ cm$ and their width in the vertical direction is b=6 cm. The length of the middle plate is $l_0 = 8.4\ cm$ and of the side plates is $l_1 = l_2 = 14\ cm$, except for the motion experiment of gait 4, for which one side plate has been replaced to $l_1 = 10.5\ cm$ in order to break the front-back symmetry. Two servo motors (SANWA, SPEC-GP) are actuating the joint angles. The aluminum plates are immersed in a viscous fluid, while the motors are placed on a flotation cell made of foam. The role of the flotation cell is to maintain planar motion of the swimmer in horizontal plane, as well as holding the motors outside of the fluid. The fluid is highly viscous silicone oil with kinematic viscosity of $\nu = 60000\ cSt$ and specific gravity of 0.976. Characteristic angular velocity of the joints is ω=$0.24 rad/sec$. The characteristic velocity is taken as the mean velocity of the side link due to joint rotation, i.e. v=$0.5 l_2 \omega$=$0.0168 m/s$. Thus, the characteristic Reynolds number for the experiments is estimated as Re=$vl/\nu \approx 0.039$. This verifies that the motion is under the regime of low Reynolds number hydrodynamics, so that inertial effects are indeed negligible even for this macro-robotic system due to the high viscosity and slow motions. The experiments were conducted in a rounded container with diameter of $1m$. The swimmer was placed close to the center of the container in order to minimize the effect of the walls, since the theoretical model assumed unbounded fluid domain. An infrared Optitrack Flex V:100 camera was used for measurements of the swimmer's planar motion. The camera tracks two reflectors attached to the motors in sampling rate of $100Hz$, and raw measurements are filtered using a 5-point moving average and processed using MATLAB for calculation of the body motion $x(t), y(t)$ and $\theta(t)$. The gaits of the joint angles $\phi_1(t), \phi_2(t)$ were generated by MATLAB, and angle commands were sent to a DSP controller by using MATLAB's Simulink toolbox. The motors were connected to the DSP controller via cable which was hung on top of the robot in order to minimize its influence on disturbance forces applied to the swimmer.

A. Experimental Results

Motion experiments under four different gaits were conducted. The first gait is the square-shaped gait 1 shown in Fig. 1(b), with stroke amplitude ϕ_0=55° and period time T=16 sec. The second gait is the rectilinear figure-eight gait 2, shown in the dashed line in Fig. 5(b), with stroke amplitude ϕ_0=65° and period time T=32 sec. The third gait is the rectilinear figure-eight gait 3, shown in the dashed line in Fig. 5(c), with stroke amplitude ϕ_0=50° and period time T=32 sec. Finally, the fourth gait for the swimmer with

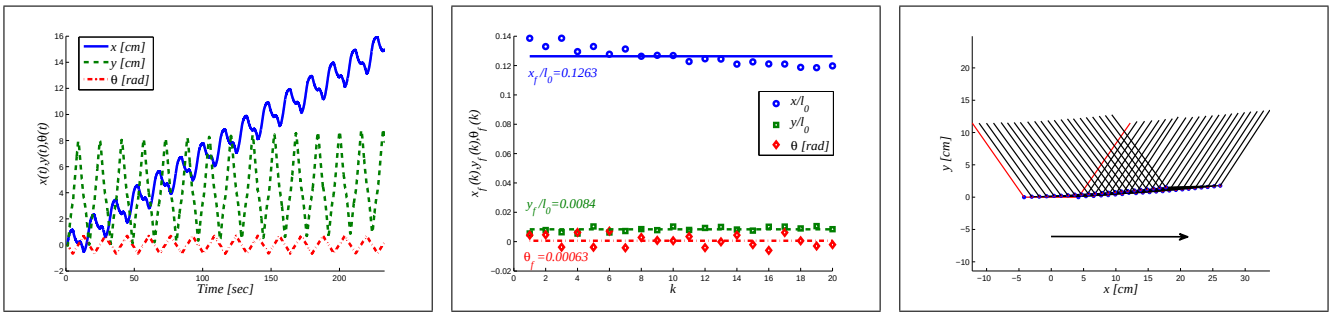

(a) (b) (c)

Fig. 11: Experimental results of gait 1 with $\phi_0 = 55°$. (a) Time plots of body motion $x(t), y(t), \theta(t)$. (b) Net motion (x_f, y_f, θ_f) vs. period index k, mean values appear in labels. (c) Motion snapshots of the swimmer in $x-y$ plane, once every period.

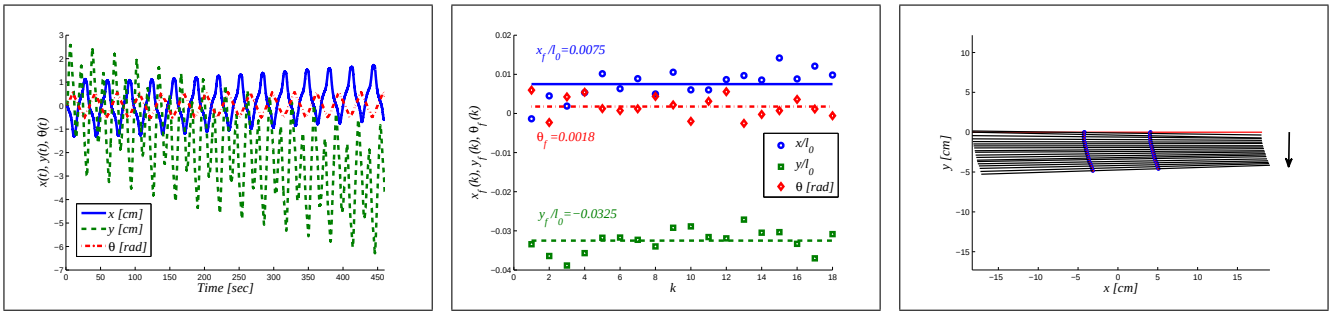

(a) (b) (c)

Fig. 12: Experimental results of gait 2 with $\phi_0 = 65°$. (a) Time plots of body motion $x(t), y(t), \theta(t)$. (b) Net motion (x_f, y_f, θ_f) vs. period index k, mean values appear in labels. (c) Motion snapshots of the swimmer in $x-y$ plane, once every period.

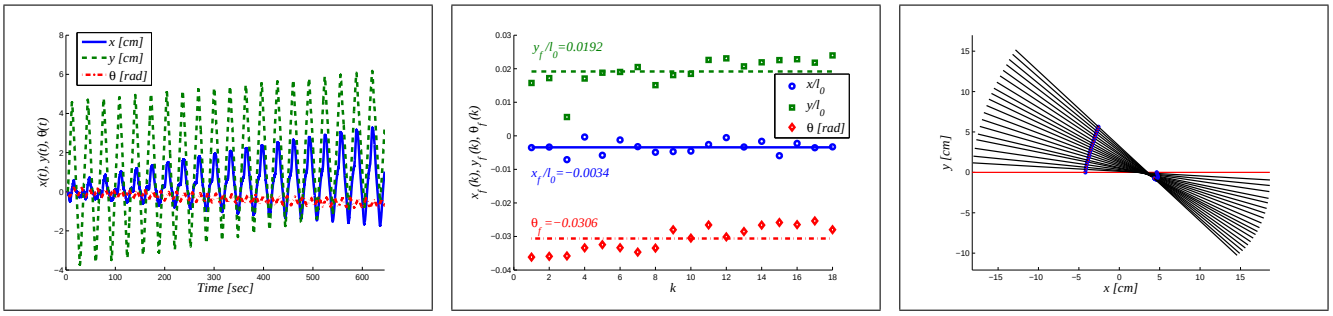

(a) (b) (c)

Fig. 13: Experimental results of gait 3 with $\phi_0 = 50°$. (a) Time plots of body motion $x(t), y(t), \theta(t)$. (b) Net motion (x_f, y_f, θ_f) vs. period index k, mean values appear in labels. (c) Motion snapshots of the swimmer in $x-y$ plane, once every period.

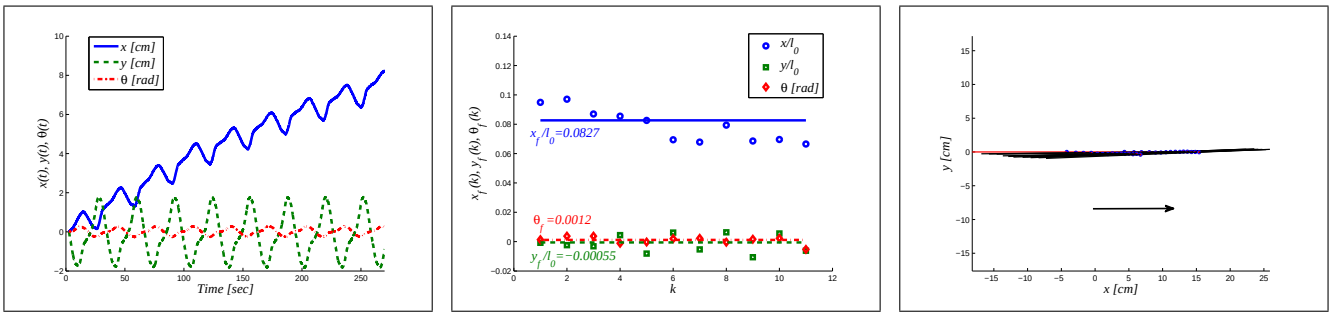

(a) (b) (c)

Fig. 14: Experimental results of gait 4 with $\phi_0 = 50°$. (a) Time plots of body motion $x(t), y(t), \theta(t)$. (b) Net motion (x_f, y_f, θ_f) vs. period index k, mean values appear in labels. (c) Motion snapshots of the swimmer in $x-y$ plane, once every period.

	Gait 1	Gait 2	Gait 3	Gait 4
x_f/l_0 - experiment (mean $\pm$ st. deviation)	$\mathbf{0.1263}$ ± 0.0061	0.0075 ± 0.0037	0.0034 ± 0.0019	$\mathbf{0.0827}$ ± 0.0113
x_f/l_0 - simulation	$\mathbf{0.2686}$	0	$8.721 \cdot 10^{-5}$	$\mathbf{0.0606}$
y_f/l_0 - experiment (mean $\pm$ st. deviation)	0.0084 ± 0.0016	$\mathbf{0.0325}$ ± 0.0030	0.0192 ± 0.0043	0.00055 ± 0.0061
y_f/l_0 - simulation	0	$\mathbf{0.04866}$	0.002503	$1.793 \cdot 10^{-4}$
θ_f $[rad]$ - experiment (mean $\pm$ st. deviation)	0.00063 ± 0.0041	0.0018 ± 0.0027	$\mathbf{0.0306}$ ± 0.0038	0.0012 ± 0.0026
θ_f $[rad]$ - simulation	0	0	$\mathbf{0.06966}$	0

TABLE II: Comparison of experimental measurement of net body motion to numerical simulations for gaits 1-4. The values in **bold** denote the dominant components for each gait.

$l_1 \neq l_2$ is the skewed figure-eight gait 4 shown in Fig. 9(a), with stroke amplitude ϕ_0=50° and period time T=32 $sec.$ Video movie files of motion experiments under gaits 1,2 and 3 (speeded up by $\times\{8, 6, 32\}$, respectively) appear in the supplementary material.

The results of the four motion experiments are shown in Figures 11-14. The position and orientation $x(t)$, $y(t)$ and $\theta(t)$ obtained from filtering and processing the markers' position measurements are plotted in Figures 11-14(a). The net body motion for each period was calculated according to the formula $\mathbf{A}_\gamma[k] = \mathbf{A}(\mathbf{q}_{k-1})^{-1}\mathbf{A}(\mathbf{q}_k)$, where $\mathbf{q}_k$=$\mathbf{q}(t$=$kT)$ and k=$0, 1, 2\ldots$ is the discrete period index. That is, $\mathbf{A}_\gamma[k]$ represents the body motion due to application of the gait at the k^{th} period, expressed with respect to a reference frame which is attached to the swimmer's body at its position right after the previous step (this is equivalent to resetting the initial conditions to zero after each step). The net body motion x_f, y_f, θ_f as a function of the step index k are shown in Figures 11-14(b), as obtained from the filtered position measurements. Mean value and standard deviation across multiple periods were also computed, and appear in the text of the plots (mean only) and in Table II. Finally, motion snapshots of the swimmer's configuration in $x-y$ plane at the end of each period as extracted from the filtered position measurements are shown in Figures 11-14(c). The results of the net body motion for each gait are summarized in Table II, and compared to theoretical results of numerical simulation for the three-link swimmer with slender links whose lengths l_0, l_1, l_2 are identical to the plate lengths, under the same gaits as in the experiments. The bold values in Table II denote the dominant components of net motion for each gait.

The experimental results summarized in Table II are in excellent qualitative agreement and reasonable quantitative agreement with the theoretical results of numerical simulations. It can be seen that the dominant directions of net body motion under gaits $\{1, 2, 3, 4\}$ are $\{x, y, \theta, x\}$, respectively, and that motion in the other directions is significantly smaller ($1-2$ orders of magnitude), as predicted by the theory. The values of dominant components of net motion in the experiments under gaits $1-4$ differ from corresponding values in the numerical simulations, yet they are in the same order of magnitude. Perhaps the main reasons for these difference are the fact that the links of the robotic swimmer are thin plates rather than slender rods as in the theoretical model, as well as the effect of added drag of the floatation cell which was not accounted by the simulation. The standard deviations of measured values of net motion in the dominant directions is in percentage of $\{4.8\%\ , 9.2\%\ , 12.4\%,\ 13.7\%\}$. This indicates that there were imperfections in the repeatability of net body motion between periods. Another significant discrepancy between the simulation and experiment is the net motion under gait 3 of nearly pure rotation, in which the net translation in the experiment is in the same order of magnitude as net rotation, in contrast to a much smaller ratio in the numerical simulations. This observation is even more evident in the motion snapshots in Figure 13(c), where it can be clearly seen that the swimmer rotates about a point which is in notable offset from the middle link's center. Nevertheless, the fact that the swimmer's center of rotation is very close to being a fixed body point indicates a fair level of repeatability. There are many possible explanations to all the discrepancies and the repeatability imperfections. The most probable reasons involve physical effects that were not considered in the theoretical model, listed as follows. First, despite the efforts made to keep slackness of the cable connecting the swimmer's motors to the DSP controller, its tension applies external forces on the swimmer which had a non-negligible cumulative effect. Second, the large strokes of the side plates caused significant shifts in the horizontal position of swimmer's center of mass, which, in, turn, induced lateral tilting oscillations of the floatation foam, violating the assumption of purely planar motion. Third, the distance of the swimmer from the walls of container was changing during motion and caused violations of the assumed symmetries, while hydrodynamic interaction of the walls and the swimmer was completely neglected in the model. Finally, other unmodelled effects are hydrodynamic interaction between the links for large stroke amplitudes, drag force on the floatation cell, and the influence of inertial forces.

In order to test the dependence of net body motion on stroke amplitude, another set of motion experiments has been conducted under the square gait 1, where the stroke amplitude ϕ_0 has been varied from 20° to 50° with 5°-increments. For each value of ϕ_0, the net forward motion x_f has been measured and averaged over 10-20 periods. The measurements were compared to theoretical predictions of numerical simulation for a swimmer model with slender links having the same lengths. The results are plotted in Fig. 15, where the solid line indicates numerical simulations, the dashed line indicates experimental measurements, and the error bars denote the standard deviation for each experiment. It can be seen that

despite the difference in the link's shape, the experimental and theoretical results are in the same order of magnitude. One unexplained finding is that the curve of the experimental measurement is not monotonically increasing around ϕ_0=40°, in contrast to the theoretical prediction. It is known from numerical simulations for larger values of ϕ_0 that Purcell's swimmer has an optimal stroke amplitudes at which the displacement x_f is maximized and that for larger amplitudes x_f even reverses its direction [20], [37]. These effects were not corroborated by our experiments, since they require larger stroke amplitudes which were not implementable due to mechanical limitations of the servo motors' assembly. Moreover, the experimental measurements shown in Fig. 15 also do not capture the scaling of x_f as $O(\varepsilon^2)$ for small stroke amplitudes. The reason is that limitations of the optical tracking system implied that for gaits with small values of ϕ_0 below 20°, inaccuracies and noises in the position measurements became too large compared to the net displacement, rendering such measurements unreliable.

VIII. Conclusion

In this work we have analyzed symmetries and gaits of shape changes for Purcell's three-link microswimmer model. Symmetric gaits have been proposed, that generate net translation in the body's prinicpal directions as well as almost pure net rotation. Gaits that generate pure translation were also proposed for more realistic microswimmer models with a single axis of symmetry. Scaling of the net body motion under small-amplitude gaits has been analyzed by using perturbation expansion. The results were demonstrated by numerical simulations and by controlled motion experiments of a macro-scale robotic swimmer in a highly viscous fluid. Importantly, the theoretical results are not restricted by the choice to use the approximation of resistive force theory, and all the symmetry arguments apply also under more accurate solutions of Stokes equations, as long as the swimmer retains its geometric symmetries. Moreover, the results are also not limited to microswimmers, and apply to any robotic three-link locomotion system such as large swimmers in a perfect fluid [26]–[28] and the kinematic snake [31]. Extension of the theory to multi-link swimmers, such as the discretization of a deformable filament [34], [37] remains a challenging open problem.

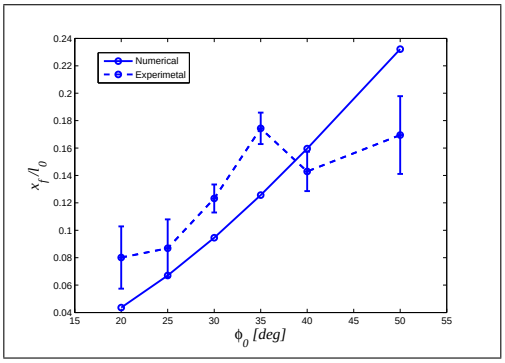

Fig. 15: Net forward motion x_f as a function of stroke amplitude ϕ_0 under the square gait. Solid line - numerical simulations. Dashed line - mean value of experimental results, error bars denote one standard deviation.

We now discuss some limitations of our work and list some possible extensions. First, we note that the gaits derived here using symmetry considerations are by no means optimal. A possible way to compute optimal gaits, which is a direct extension of [23], is to formulate the time-periodic functions $\phi_i(t)$ as truncated Fourier series that respect the particular symmetries of the gait, and then numerically optimize the discrete set of series coefficients in order maximize a chosen cost function such as net displacement or energetic efficiency. Another way is to treat the problem using optimal control approach, i.e. Pontryagin's principle, cf. [24], [34]. Notably, the swimmer's structure, e.g. ratio of links' lengths, also has a substantial effect on performance and thus it could also be optimized, as already shown in [23], [24].

As most of the works on microswimmers models and robotic locomotion systems, our work is heavily based on two crucial assumptions. The first assumption is that the kinematic shape of the swimmer can be directly controlled, and the second is the invariance of the dynamics with respect to rigid body motion, i.e. gauge symmetry. The latter is is implied by assuming an unbounded fluid domain without any external boundary conditions. When one considers more realistic models of mechanical actuation, relaxing the first assumption, other interesting issues must be taken into account. For example, in the three-link swimmer under controlled actuation torques at the joint, one has to carefully choose the time profiles of the control torques in order to induce periodic solutions of the shape kinematics which are orbitally stable under perturbations without using feedback [40].

When the gauge symmetry assumption is relaxed by considering, for instance, a swimmer near an infinite no-slip wall, the nice structure of principal connections for the body velocities no longer exists. Thus, one has to consider symmetries with respect to the wall in order to generate gaits of shape changes that induce asymptotic convergence to motion of net translation at a fixed distance from the wall [41]. In other types of boundaries such as a circular domain [42], gaps in a wall [43], and free surface [44], the microswimmer's dynamics becomes even more interesting.

Other related works in which these two key assumptions are violated are as follows. The work [45] studies Purcell's swimmer with one actuated joint angle and one passive joint with a torsion spring which models an elastic tail. The work [46] studies the motion of a two-link swimmer with a bottom-heavy link, which is influenced by an aligning torque due to gravity. The work [47] studies a two-link swimmer with one magnetic link that is actuated by applying an oscillating external magnetic field. This two-link magnetic swimmer has recently been realized and manufactured in micron-scale [9], inspired by previous work of [8]. In these types of microswimmers the dynamics is no longer time-invariant, and thus actuation of a single periodic input is sufficient for generating net motion. Moreover, relation between the actuation frequency and the swimmer's characteristic time scales has a substantial effect on the net motion.

To summarize, the research on microswimmers dynamics and control can be extended in many directions, including theoretical modeling as well as micro-scale experiments. The analysis of structural symmetries of the dynamics and their potential use for gait generation, control and stabilization is expected to play a central role in future works in all these directions.

APPENDIX - PROOFS OF TECHNICAL DETAILS

Proof of Proposition 1

Let $\mathbf{q}_f = (x_f, y_f, \theta_f)^T$ denote the net body motion under initial conditions $\mathbf{q}(0) = (x_0, y_0, \theta_0)^T$, and let $\tilde{\mathbf{q}}_f = (\tilde{x}_f, \tilde{y}_f, \tilde{\theta}_f)^T$ denote the net body motion under zero initial conditions $\mathbf{q}(0)$=0. The motion $\mathbf{q}(t)$ is obtained by integrating the equation of motion (6), which satisfies the decomposition (7). Due to the special structure of $\mathbf{D}(\theta)$ in (7), the equation for $\dot{\theta}(t)$ is independent of $\mathbf{q}$ and can be directly integrated in order to obtain:

$$\theta(t) = \theta_0 + \int_0^t \mathbf{G}_3(\boldsymbol{\Phi}(t'))\dot{\boldsymbol{\Phi}}(t')dt' \triangleq \theta_0 + \tilde{\theta}(t)$$

where $\mathbf{G}_3(\boldsymbol{\Phi})$ is the third row of $\mathbf{G}(\boldsymbol{\Phi})$ and $\tilde{\theta}(t)$ is the solution under zero initial condition. The net body position at t=T can then be obtained as

$$\begin{bmatrix} x_f \\ y_f \end{bmatrix} = \begin{bmatrix} x_0 \\ y_0 \end{bmatrix} + \int_0^T \begin{bmatrix} \cos(\theta_0+\tilde{\theta}(t)) & -\sin(\theta_0+\tilde{\theta}(t)) \\ \sin(\theta_0+\tilde{\theta}(t)) & \cos(\theta_0+\tilde{\theta}(t)) \end{bmatrix} \begin{bmatrix} \mathbf{G}_1(\boldsymbol{\Phi}(t)) \\ \mathbf{G}_2(\boldsymbol{\Phi}(t)) \end{bmatrix} \dot{\boldsymbol{\Phi}}(t)dt$$
$$= \begin{bmatrix} x_0 \\ y_0 \end{bmatrix} + \begin{bmatrix} \cos\theta_0 & -\sin\theta_0 \\ \sin\theta_0 & \cos\theta_0 \end{bmatrix} \cdot \int_0^T \begin{bmatrix} \cos\tilde{\theta}(t) & -\sin\tilde{\theta}(t) \\ \sin\tilde{\theta}(t) & \cos\tilde{\theta}(t) \end{bmatrix} \begin{bmatrix} \mathbf{G}_1(\boldsymbol{\Phi}(t)) \\ \mathbf{G}_2(\boldsymbol{\Phi}(t)) \end{bmatrix} \dot{\boldsymbol{\Phi}}(t)dt$$
$$= \begin{bmatrix} x_0 \\ y_0 \end{bmatrix} + \begin{bmatrix} \cos\theta_0 & -\sin\theta_0 \\ \sin\theta_0 & \cos\theta_0 \end{bmatrix} \begin{bmatrix} \tilde{x}_f \\ \tilde{y}_f \end{bmatrix}$$

where $\mathbf{G}_i(\boldsymbol{\Phi})$ is the i^{th} row of $\mathbf{G}(\boldsymbol{\Phi})$ for i=1, 2. This relation can be written in the form of a homogeneous rigid-body transformation matrix as:

$$\mathbf{A}(\boldsymbol{\psi}(\gamma, \mathbf{q}_0)) = (x_f, y_f, \theta_f)^T = \begin{bmatrix} \cos(\theta_0+\theta) & -\sin(\theta_0+\theta) & x_0 + \tilde{x}_f\cos\theta_0 - \tilde{y}_f\sin\theta_0 \\ \sin(\theta_0+\theta) & \cos(\theta_0+\theta) & y_0 + \tilde{x}_f\sin\theta_0 + \tilde{y}_f\cos\theta_0 \\ 0 & 0 & 1 \end{bmatrix},$$

which is precisely equivalent to the relation (11) . □

Proof of Theorem 1

Let $\mathbf{q}_f$=$(x_f, y_f, \theta_f)^T$ denote the net body motion under the shape trajectory $\gamma = \boldsymbol{\Phi}(t)$, which is obtained by integrating (6) as

$$\mathbf{q}_f = \boldsymbol{\psi}(\gamma, 0) = \int_0^T \mathbf{D}(\theta(t))\mathbf{G}(\boldsymbol{\Phi}(t))\dot{\boldsymbol{\Phi}}(t)dt\ .$$

Let $\tilde{\mathbf{q}}_f = (\tilde{x}_f, \tilde{y}_f, \tilde{\theta}_f)^T$ denote the net body motion under the reflected shape trajectory $F_1(\gamma)$= $-\boldsymbol{\Phi}(t)$. Using the velocity symmetry f_1 from (8) then gives

$$\boldsymbol{\psi}(F_1(\gamma), 0) = \int_0^T \mathbf{D}(\tilde{\theta}(t))\mathbf{G}(-\boldsymbol{\Phi}(t))(-\dot{\boldsymbol{\Phi}}(t))dt$$
$$= -\int_0^T \mathbf{D}(\tilde{\theta}(t))\mathbf{G}(-\boldsymbol{\Phi}(t))\dot{\boldsymbol{\Phi}}(t)dt$$
$$= -\int_0^T \mathbf{D}(\tilde{\theta}(t)) \begin{bmatrix} -1 & 0 & 0 \\ 0 & 1 & 0 \\ 0 & 0 & 1 \end{bmatrix} \mathbf{G}(\boldsymbol{\Phi}(t))\dot{\boldsymbol{\Phi}}(t)dt$$
$$= \int_0^T \begin{bmatrix} \cos(\tilde{\theta}(t)) & \sin(\tilde{\theta}(t)) & 0 \\ \sin(\tilde{\theta}(t)) & -\cos(\tilde{\theta}(t)) & 0 \\ 0 & 0 & -1 \end{bmatrix} \mathbf{G}(\boldsymbol{\Phi}(t))\dot{\boldsymbol{\Phi}}(t)dt$$

where $\tilde{\theta}(t)$ is the body orientation angle during motion under the shape trajectory $F_1(\gamma)$. Using the velocity symmetry f_1 from (8), $\tilde{\theta}(t)$ is related to $\theta(t)$, which is the body angle under shape trajectory γ, according to:

$$\tilde{\theta}(t) = -\int_0^t \mathbf{G}_3(\boldsymbol{\Phi}(t'))\dot{\boldsymbol{\Phi}}(t')dt' = -\theta(t).$$

The net translation $\tilde{x}_f$ and $\tilde{y}_f$ can then be obtained as

$$\begin{bmatrix} \tilde{x}_f \\ \tilde{x}_f \end{bmatrix} = \int_0^T \begin{bmatrix} \cos\tilde{\theta}(t) & \sin\tilde{\theta}(t) \\ \sin\tilde{\theta}(t) & -\cos\tilde{\theta}(t) \end{bmatrix} \begin{bmatrix} \mathbf{G}_1(\boldsymbol{\Phi}(t)) \\ \mathbf{G}_2(\boldsymbol{\Phi}(t)) \end{bmatrix} \dot{\boldsymbol{\Phi}}(t)dt$$
$$= \int_0^T \begin{bmatrix} \cos\theta(t) & -\sin\theta(t) \\ -\sin\theta(t) & -\cos\theta(t) \end{bmatrix} \begin{bmatrix} \mathbf{G}_1(\boldsymbol{\Phi}(t)) \\ \mathbf{G}_2(\boldsymbol{\Phi}(t)) \end{bmatrix} \dot{\boldsymbol{\Phi}}(t)dt = \begin{bmatrix} x_f \\ -y_f \end{bmatrix}$$

These relations can be written in terms of homogeneous matrix transformation as: $\mathbf{A}_{F_1(\gamma)} = \begin{bmatrix} \cos\theta_f & \sin\theta & x_f \\ -\sin\theta_f & \cos\theta_f & -y_f \\ 0 & 0 & 1 \end{bmatrix}$. □

Proof of Theorem 2

Let $\mathbf{q}_f$=$(x_f, y_f, \theta_f)^T$ denote the net body motion under the shape trajectory $\gamma = \boldsymbol{\Phi}(t)$, and let $\theta(t)$ denote the body angle during motion. Similarly, let $\tilde{\mathbf{q}}_f = (\tilde{x}_f, \tilde{y}_f, \tilde{\theta}_f)^T$ denote the net body motion under the reflected shape trajectory $F_2(\gamma)$=$\mathbf{S}\boldsymbol{\Phi}(t)$, and let $\tilde{\theta}(t)$ denote the body angle during motion. Using the velocity symmetry f_2 from (9) then gives

$$\tilde{\mathbf{q}}_f = \boldsymbol{\psi}(F_2(\gamma), 0) = \int_0^T \mathbf{D}(\tilde{\theta}(t))\mathbf{G}(\mathbf{S}\boldsymbol{\Phi}(t))\mathbf{S}\dot{\boldsymbol{\Phi}}(t)dt$$
$$= \int_0^T \mathbf{D}(\tilde{\theta}(t)) \begin{bmatrix} -1 & 0 & 0 \\ 0 & 1 & 0 \\ 0 & 0 & -1 \end{bmatrix} \mathbf{G}(\boldsymbol{\Phi}(t))\mathbf{S}^2\dot{\boldsymbol{\Phi}}(t)dt$$
$$= \int_0^T \begin{bmatrix} -\cos\tilde{\theta}(t) & -\sin\tilde{\theta}(t) & 0 \\ -\sin\tilde{\theta}(t) & \cos\tilde{\theta}(t) & 0 \\ 0 & 0 & -1 \end{bmatrix} \mathbf{G}(\boldsymbol{\Phi}(t))\dot{\boldsymbol{\Phi}}(t)dt.$$

The relation between $\tilde{\theta}(t)$ and $\theta(t)$ is given by

$$\tilde{\theta}(t) = \int_0^t \mathbf{G}_3(\mathbf{S}\boldsymbol{\Phi}(t'))\mathbf{S}\dot{\boldsymbol{\Phi}}(t')dt' = -\theta(t).$$

The net translation $\tilde{x}_f$ and $\tilde{y}_f$ can then be obtained as

$$\begin{aligned}
&\begin{bmatrix} x_f \\ y_f \end{bmatrix} = \\
&= \int_0^T \begin{bmatrix} -\cos\tilde{\theta}(t) & -\sin\tilde{\theta}(t) \\ -\sin\tilde{\theta}(t) & \cos\tilde{\theta}(t) \end{bmatrix} \begin{bmatrix} \mathbf{G}_1(\boldsymbol{\Phi}(t)) \\ \mathbf{G}_2(\boldsymbol{\Phi}(t)) \end{bmatrix} \dot{\boldsymbol{\Phi}}(t)dt \\
&= \int_0^T \begin{bmatrix} -\cos\theta(t) & \sin\theta(t) \\ \sin\theta(t) & \cos\theta(t) \end{bmatrix} \begin{bmatrix} \mathbf{G}_1(\boldsymbol{\Phi}(t)) \\ \mathbf{G}_2(\boldsymbol{\Phi}(t)) \end{bmatrix} \dot{\boldsymbol{\Phi}}(t)dt \\
&= \begin{bmatrix} -x_f \\ y_f \end{bmatrix}
\end{aligned}$$

These relations can be written in terms of homogeneous matrix transformation as: $\mathbf{A}_{F_2(\gamma)} = \begin{bmatrix} \cos\theta_f & \sin\theta_f & -x_f \\ -\sin\theta_f & \cos\theta_f & y_f \\ 0 & 0 & 1 \end{bmatrix}$. □

Proof of Theorem 3

Due to the structure of the equation of motion (6), it is clear that if $\mathbf{q}(t)$ is a solution of (6) under shape change $\gamma = \boldsymbol{\Phi}(t)$, then $\mathbf{q}(T-t)$ is a solution of (6) under the reversed shape change $\gamma' = F_3(\gamma) = \boldsymbol{\Phi}(T-t)$. Denoting $\mathbf{q}_0 = \mathbf{q}(0)$ and $\mathbf{q}_T = \mathbf{q}(T)$, one obtains that $\mathbf{q}_T = \boldsymbol{\psi}(\gamma, \mathbf{q}_0)$ and $\mathbf{q}_0 = \boldsymbol{\psi}(\gamma', \mathbf{q}_T)$. Using the gauge symmetry relation (11) from Proposition 1 then yields

$$\begin{aligned}
\mathbf{A}(\mathbf{q}_0) &= \mathbf{A}(\boldsymbol{\psi}(\gamma', \mathbf{q}_T)) = \mathbf{A}(\mathbf{q}_T)\mathbf{A}(\boldsymbol{\psi}(\gamma', 0)) \\
&= \mathbf{A}(\boldsymbol{\psi}(\gamma, \mathbf{q}_0))\mathbf{A}(\boldsymbol{\psi}(\gamma', 0)).
\end{aligned}$$

Setting $\mathbf{q}_0 = 0$ then gives

$$\mathbf{A}(0) = \mathbf{I} = \mathbf{A}(\boldsymbol{\psi}(\gamma, 0))\mathbf{A}(\boldsymbol{\psi}(\gamma', 0)) = \mathbf{A}_\gamma \mathbf{A}_{\gamma'},$$

where $\mathbf{I}$ is the identity matrix. This implies that $\mathbf{A}_{\gamma'} = \mathbf{A}_\gamma^{-1}$. □

Proof of Theorems 4-6

Consider a shape trajectory $\gamma_1 = \varepsilon\boldsymbol{\Phi}(t)$, which is one part of a closed loop. The solution for the body angle $\theta(t)$ is given by

$$\theta(t) = \int_0^t \mathbf{G}_3(\varepsilon\boldsymbol{\Phi}(t'))\varepsilon\dot{\boldsymbol{\Phi}}(t')dt'. \tag{26}$$

In order to solve (26) using perturbation expansion [35], $\theta(t)$ is expressed as a power series in the small amplitude ε as $\theta(t) = \varepsilon\theta_1(t) + \varepsilon^2\theta_2(t) + \varepsilon^3\theta_3(t) + \cdots$. The matrix $\mathbf{G}(\boldsymbol{\Phi})$ can then be expanded about $\boldsymbol{\Phi}=0$ as a power series in its arguments ϕ_1 and ϕ_2. Finally, the expansion of (26) can be arranged into different leading orders of ε which are integrated as:

$$\begin{aligned}
\theta_1(t) &= \mathbf{G}_3(0)(\boldsymbol{\Phi}(t) - \boldsymbol{\Phi}(0)) \\
\theta_2(t) &= \int_0^t \left[\frac{d\mathbf{G}_3^T}{d\boldsymbol{\Phi}}(0)\boldsymbol{\Phi}(t')\right]^T \dot{\boldsymbol{\Phi}}(t')dt' \\
\theta_3(t) &= \frac{1}{2}\int_0^t \boldsymbol{\Phi}(t')^T[\nabla^2 G_{31}\boldsymbol{\Phi}(t') \;\; \nabla^2 G_{32}\boldsymbol{\Phi}(t')]\dot{\boldsymbol{\Phi}}(t')dt',
\end{aligned} \tag{27}$$

where G_{ij} is the i,j-element of $\mathbf{G}(\boldsymbol{\Phi})$ and the operator ∇^2 represents the Hessian matrix containing second-order derivatives with respect to ϕ_1 and ϕ_2, evaluated at $\boldsymbol{\Phi}=0$.

The net translation under γ_1 can then be obtained by integrating (6) and using (7) as:

$$\begin{bmatrix} x \\ y \end{bmatrix} = \int_0^T \begin{bmatrix} \cos\theta(t) & -\sin\theta(t) \\ \sin\theta(t) & \cos\theta(t) \end{bmatrix} \begin{bmatrix} \mathbf{G}_1(\varepsilon\boldsymbol{\Phi}(t)) \\ \mathbf{G}_2(\varepsilon\boldsymbol{\Phi}(t)) \end{bmatrix} \varepsilon\dot{\boldsymbol{\Phi}}(t)dt. \tag{28}$$

x and y are expressed as a power series in ε as

$$\begin{aligned}
x &= \varepsilon x_1 + \varepsilon^2 x_2 + \varepsilon^3 x_3 + \dots \\
y &= \varepsilon y_1 + \varepsilon^2 y_2 + \varepsilon^3 y_3 + \dots
\end{aligned}$$

The trigonometric terms of the rotation matrix in (28) can be expanded as power series in $\theta(t)$ and then in ε as

$$\begin{aligned}
\cos\theta(t) &= 1 - \frac{1}{2}\theta^2 + O(\theta^4) = 1 - \frac{1}{2}\varepsilon^2\theta_1^2(t) + O(\varepsilon^3) \\
\sin\theta(t) &= \theta + O(\theta^3) = \varepsilon\theta_1(t) + \varepsilon^2\theta_2(t) + O(\varepsilon^3).
\end{aligned}$$

Expanding the rows of $\mathbf{G}(\boldsymbol{\Phi})$ in (28) as Taylor series in ϕ_1 and ϕ_2 and substituting (27), leading order expressions for x and y are obtained as

$$\begin{aligned}
x_1 &= \mathbf{G}_1(0)(\boldsymbol{\Phi}(T) - \boldsymbol{\Phi}(0)) \\
x_2 &= \int_0^T \left[\frac{d\mathbf{G}_1^T}{d\boldsymbol{\Phi}}(0)\boldsymbol{\Phi}(t)\right]^T \dot{\boldsymbol{\Phi}}(t) - \theta_1(t)\mathbf{G}_2(0)\dot{\boldsymbol{\Phi}}(t)dt \\
y_1 &= \mathbf{G}_2(0)(\boldsymbol{\Phi}(T) - \boldsymbol{\Phi}(0)) \\
y_2 &= \int_0^T \left[\frac{d\mathbf{G}_2^T}{d\boldsymbol{\Phi}}(0)\boldsymbol{\Phi}(t)\right]^T \dot{\boldsymbol{\Phi}}(t) \\
&\quad + (\boldsymbol{\Phi}(t) - \boldsymbol{\Phi}(0))^T\mathbf{G}_3^T(0)\mathbf{G}_1(0)\dot{\boldsymbol{\Phi}}(t)dt \\
y_3 &= \int_0^T \left(\theta_1(t)\left[\frac{d\mathbf{G}_1^T}{d\boldsymbol{\Phi}}(0)\boldsymbol{\Phi}(t)\right]^T + \theta_2(t)\mathbf{G}_1(0)\right. \\
&\quad \left. + \boldsymbol{\Phi}^T(t)[\nabla^2 G_{21}\boldsymbol{\Phi}(t) \;\; \nabla^2 G_{22}\boldsymbol{\Phi}(t)] - \frac{1}{2}\theta_1^2(t)\mathbf{G}_2(0)\right)\dot{\boldsymbol{\Phi}}dt
\end{aligned} \tag{29}$$

We now analyze the ε-order of net body motion x, y, θ for the sub-paths γ_1 in each of the gaits 1-5, according to equations (27) and (29). Under gaits 1-4, the swimmer satisfies the axial symmetry f_1 in (8), which implies that $\mathbf{G}_1(\boldsymbol{\Phi}) = -\mathbf{G}_1(-\boldsymbol{\Phi})$, and thus one obtains that $\mathbf{G}_1(0)=0$. Therefore, (29) implies that $x_1=0$. Under gait 5, axial symmetry f_1 no longer holds. Nevertheless, the sub-path γ_1 under this gait satisfies $\boldsymbol{\Phi}(0) = \boldsymbol{\Phi}(T)$, and (29) again implies that $x_1=0$. Thus, one concludes that $x = O(\varepsilon^2)$ under all gaits 1-5.

Under gaits 1-4, the axial symmetry f_1 in (8) implies that $\mathbf{G}_3(\boldsymbol{\Phi}) = \mathbf{G}_3(-\boldsymbol{\Phi})$, and thus one obtains that $\frac{d\mathbf{G}_3^T}{d\boldsymbol{\Phi}}(0)=0$. Thus, (27) implies that $\theta_2(T)=0$. Nevertheless, $\theta_1(T)$ in (27) does not necessarily vanish for all gaits. For gaits 1,2 and 4 one obtains that $\theta_1(T) \neq 0$ in general. In gait 3, conditions on the endpoints of γ_1 are $\phi_1(0)=\phi_2(0)=0$ and $\phi_1(T)=\phi_2(T)$, and front-back symmetry (9) implies that $G_{31}(0) = -G_{32}(0)$. Invoking (27), one obtains that $\theta_1(T)=0$. In gait 5, the sub-path γ_1 satisfies $\boldsymbol{\Phi}(0) = \boldsymbol{\Phi}(T)$, and (27) implies that $\theta_1(T)=0$. Same holds for gait 4 in the special case where

$\boldsymbol{\Phi}(0) = \boldsymbol{\Phi}(T)$=0. Thus, one concludes that $\theta(T)$ is of order $O(\varepsilon)$ for gaits 1,2 and 4, $O(\varepsilon^2)$ for gait 5, and $O(\varepsilon^3)$ for gait 3 and the special type of gait 4 where $\boldsymbol{\Phi}(0) = \boldsymbol{\Phi}(T)$=0.

For gaits 1,3 and 4 one obtains that $y_1 \neq 0$ in general. In gait 2, conditions on the endpoints of γ_1 are $\phi_1(0)$=$\phi_2(0)$=0 and $\phi_1(T)$= $-$ $\phi_2(T)$, and front-back symmetry (9) implies that $G_{21}(0)$=$G_{22}(0)$. Invoking (27), one obtains that y_1=0. In gait 5, the sub-path γ_1 satisfies $\boldsymbol{\Phi}(0) = \boldsymbol{\Phi}(T)$, and (29) implies that y_1=0. Same holds for gait 4 in the special case where $\boldsymbol{\Phi}(0) = \boldsymbol{\Phi}(T)$=0. As for y_2, recall that under gaits 1-4 the axial symmetry f_1 in (8) implies that $\mathbf{G}_2(\boldsymbol{\Phi})$=$\mathbf{G}_2(-\boldsymbol{\Phi})$, and thus one obtains that $\frac{d\mathbf{G}_2^T}{d\boldsymbol{\Phi}}(0)$=0. Since $\mathbf{G}_1(0)$=0 under this symmetry, (29) implies that y_2=0. For gait 5, we now prove that y_2=0 as well. It can be verified that the front-back symmetry (9) implies that the two matrices $\frac{d\mathbf{G}_2^T}{d\boldsymbol{\Phi}}(0)$ and $\mathbf{G}_3^T(0)\mathbf{G}_1(0)$ are symmetric. Therefore, the expression for y_2 in (29) can be integrated as

$$y_2 = \frac{1}{2}\Bigg(\boldsymbol{\Phi}(t)^T\left[\frac{d\mathbf{G}_2^T}{d\boldsymbol{\Phi}}(0)\right]\boldsymbol{\Phi}(t) + (\boldsymbol{\Phi}(t)-\boldsymbol{\Phi}(0))^T[\mathbf{G}_3^T(0)\mathbf{G}_1(0)](\boldsymbol{\Phi}(t)-\boldsymbol{\Phi}(0))^T\Bigg)\Bigg|_0^T. \tag{30}$$

Since the endpoints of γ_1 under gait 5 satisfy $\boldsymbol{\Phi}(0) = \boldsymbol{\Phi}(T)$, (30) imples that $y_2 = 0$. Thus, one concludes that y=$O(\varepsilon)$ for gaits 1,3 and 4 and y=$O(\varepsilon^3)$ for gait 2,5 and the special type of gait 4 where $\boldsymbol{\Phi}(0) = \boldsymbol{\Phi}(T)$=0.

Finally, we consider motion under the entire loop γ for gaits 1-5 and determine the ε-orders of the net body motion (x_f, y_f, θ_f). In gait 1, according to equation (19), one obtains that y_f=θ_f=0 while x_f=$4x$ scales as ε^2. In gait 2, according to equation (21) one obtains that x_f=θ_f=0 while y_f=$4y$ scales as ε^3. In gait 3, according to (23), the net rotation under the gait γ is θ_f=4θ=$O(\varepsilon^3)$, and the net translation is

$$\begin{bmatrix} x_f \\ y_f \end{bmatrix} = \begin{bmatrix} x(1-\cos 4\theta) + y(2\sin 2\theta - \sin 4\theta) \\ -x\sin 4\theta + y(1 - 2\cos 2\theta + \cos 4\theta) \end{bmatrix} = \begin{bmatrix} x\cdot O(\theta^2) + y\cdot O(\theta^3) \\ -x\cdot O(\theta) + y\cdot O(\theta^2) \end{bmatrix} = \begin{bmatrix} O(\varepsilon^8) \\ O(\varepsilon^5) \end{bmatrix}.$$

This is precisely the scaling that appears in Table I. In gait 4, according to (24) the net rotation θ_f under the entire gait is zero, while the net translation satisfies

$$\begin{bmatrix} x_f \\ y_f \end{bmatrix} = \begin{bmatrix} x(1+\cos\theta) + y\sin\theta \\ y(1-\cos\theta) + x\sin\theta \end{bmatrix} = \begin{bmatrix} x\cdot O(1) + y\cdot O(\theta) \\ y\cdot O(\theta^2) + x\cdot O(\theta) \end{bmatrix} = \begin{bmatrix} O(\varepsilon^2) \\ O(\varepsilon^3) \end{bmatrix}. \tag{31}$$

Moreover, if the sub-path γ_1 satisfies $\boldsymbol{\Phi}(0)$=$\boldsymbol{\Phi}(T)$=0, then the net motion under γ_1 scales as x=$O(\varepsilon^2)$, y=$O(\varepsilon^3)$ and θ=$O(\varepsilon^3)$. In this case, (31) implies that x_f=$O(\varepsilon^2)$ and y_f=$O(\varepsilon^5)$. In gait 5, recall that the net motion under γ_1 scales as x=$O(\varepsilon^2)$, y=$O(\varepsilon^3)$ and θ=$O(\varepsilon^2)$. According to (25), the net rotation θ_f under the entire gait is zero, while the net translation satisfies

$$\begin{bmatrix} x_f \\ y_f \end{bmatrix} = \begin{bmatrix} x(1-\cos\theta) - y\sin\theta \\ y(1+\cos\theta) - x\sin\theta \end{bmatrix} = \begin{bmatrix} x\cdot O(\theta^2) - y\cdot O(\theta) \\ y\cdot O(1) - x\cdot O(\theta) \end{bmatrix} = \begin{bmatrix} O(\varepsilon^5) \\ O(\varepsilon^3) \end{bmatrix}.$$

□

ACKNOWLEDGMENT

This work is supported by the Israeli Science Foundation (ISF) under Grant No. 567/14. We wish to thank the undergraduate students: Nir Armony, David Fogel, Doron Gur, Ariel Nuriel and Sagi Vald from the Technion, for design and construction of the robotic three-link swimmer, performing motion experiments, and processing of the results. We also thank the anonymous reviewers for their useful comments.

REFERENCES

[1] S. D. Kelly and R. M. Murray, "Geometric phases and robotic locomotion," *Journal of Robotic Systems*, vol. 12, no. 6, pp. 417–431, 1995.
[2] J. Ostrowski and J. Burdick, "The geometric mechanics of undulatory robotic locomotion," *The International Journal of Robotics Research*, vol. 17, no. 7, pp. 683–701, 1998.
[3] J. Cortés, *Geometric, Control, and Numerical Aspects of Nonholonomic Systems*. Berlin Heidelberg: Springer-Verlag, 2002.
[4] A. M. Bloch, *Nonholonomic mechanics and control*. Springer, 2003.
[5] E. Frazzoli, M. A. Dahleh, and E. Feron, "Maneuver-based motion planning for nonlinear systems with symmetries," *IEEE Transactions on Robotics*, vol. 21, no. 6, pp. 1077–1091, December 2005.
[6] J. Koiller, R. Montgomery, and K. Ehlers, "Problems and progress in microswimming," *J. Nonlinear Science*, vol. 6, pp. 507–541, 1996.
[7] E. Lauga and T. R. Powers, "The hydrodynamics of swimming microorganisms," *Rep. Prog. Phys.*, vol. 72, p. 096601, 2009.
[8] R. Dreyfus, J. Baudry, M. l. Roper, M. Fermigier, H. A. Stone, and J. Bibette, "Microscopic artificial swimmers," *Nature*, vol. 437, pp. 862–865, 2005.
[9] B. Jang, E. Gutman, N. Stucki, B. Seitz, P. Garcia-Wendel, T. Newton, J. Pokki, O. Ergeneman, S. Pané, Y. Or, and B. J. Nelson, "Undulatory locomotion of magnetic multi-link nanoswimmers," *Submitted*, 2015.
[10] K. E. Peyer, L. Zhang, and B. J. Nelson, "Bio-inspired magnetic swimming microrobots for biomedical applications," *Nanoscale*, vol. 5, pp. 1259–1272, 2013.
[11] B. J. Nelson, I. K. Kaliakatsos, and J. J. Abbott, "Microrobots for minimally invasive medicine," *Review of Biomedical Engineering*, vol. 12, pp. 55–85, 2010.
[12] J. Happel and H. Brenner, *Low Reynolds Number Hydrodynamics*. Prentice-Hall, 1965.
[13] J. Lohéac, J.-F. Scheid, and M. Tucsnak, "Controllability and time optimal control for low reynolds numbers swimmers," *Acta Applicandae Mathematicae*, vol. 123, no. 1, pp. 175–200, 2013.
[14] F. Alouges, A. DeSimone, and A. Lefebvre, "Optimal strokes for axisymmetric microswimmers," *The European Physical Journal E: Soft Matter and Biological Physics*, vol. 28, no. 3, pp. 279–284, 2009.
[15] A. Shapere and F. Wilczek, "Geometry of self-propulsion at low Reynolds numbers," *J. Fluid Mech.*, vol. 198, pp. 557–585, 1989.
[16] G. I. Taylor., "Analysis of the swimming of microscopic organisms," *Proc. Roy. Soc. A*, vol. 209, pp. 447–461, 1951.
[17] E. M. Purcell, "Life at low Reynolds number," *Am. J. Phys.*, vol. 45, pp. 3–11, 1977.
[18] J. E. Avron, O. Kenneth, and D. H. Oakmin, "Pushmepullyou: An efficient micro-swimmer," *New J. Phys.*, vol. 7, p. 234238, 2005.
[19] A. Najafi and R. Golestanian, "Simple swimmer at low Reynolds numbers: Three linked spheres," *Phys. Rev. E*, vol. 69, pp. 062 901–062 904, 2004.
[20] L. E. Becker, S. A. Koehler, and H. A. Stone, "On self-propulsion of micro-machines at low Reynolds numbers: Purcell's three-link swimmer," *Journal of Fluid Mechanics*, vol. 490, pp. 15–35, 2003.
[21] R. G. Cox, "The motion of long slender bodies in a viscous fluid part 1. general theory," *J. Fluid Mech.*, vol. 44, pp. 791–810, 1970.

[22] J. Gray and G. J. Hancock, "The propulsion of sea-urchin spermatozoa," *J. Exp. Biol.*, vol. 32, pp. 802–814, 1955.
[23] D. Tam and A. E. Hosoi, "Optimal stroke patterns for purcell's three-link swimmer," *Physical Review Letters*, vol. 98, p. 068105, 2007.
[24] L. Giraldi, P. Martinon, and M. Zoppello., "Optimal design of the three-link Purcell swimmer," *Physical Review E*, vol. 91, p. 023012, 2015.
[25] J. E. Avron and O. Raz, "A geometric theory of swimming: Purcell's swimmer and its symmetrized cousin," *New Journal of Physics*, vol. 10, p. 063016, 2008.
[26] E. Kanso, J. E. Marsden, C. W. Rowley, and J. B. Melli-Huber, "Locomotion of articulated bodies in a perfect fluid," *Journal of Nonlinear Science*, vol. 15, no. 4, pp. 255–289, 2005.
[27] J. B. Melli, C. W. Rowley, and D. S. Rufat, "Motion planning for an articulated body in a perfect planar fluid," *SIAM Journal of Applied Dynamical Systems*, vol. 5, no. 4, pp. 650–669, 2006.
[28] R. L. Hatton and H. Choset, "Geometric swimming at low and high reynolds numbers," *IEEE Transactions on Robotics*, vol. 29, no. 3, pp. 615–624, 2013.
[29] J. P. Ostrowski, J. P. Desai, and V. Kumar, "Optimal gait selection for nonholonomic locomotion systems," *The International Journal of Robotics Research*, vol. 19, no. 3, pp. 225–237, 2000.
[30] P. Krishnaprasad and D. P. Tsakiris, "Oscillations, se (2)-snakes and motion control: A study of the roller racer," *Dynamical Systems: An International Journal*, vol. 16, no. 4, pp. 347–397, 2001.
[31] E. A. Shammas, H. Choset, and A. A. Rizzi, "Geometric motion planning analysis for two classes of underactuated mechanical systems," *The International Journal of Robotics Research*, vol. 26, no. 10, pp. 1043–1073, 2007.
[32] R. L. Hatton, H., and Choset, "Approximating displacement with the body velocity integral," in *Proc. Robotics, Science and Systems*, 2009.
[33] R. L. Hatton and H. Choset, "Geometric motion planning: The local connection, stokes theorem, and the importance of coordinate choice," *The International Journal of Robotics Research*, vol. 30, no. 8, pp. 988–1014, 2011.
[34] L. Giraldi, P. Martinon, and M. Zoppello, "Controllability and optimal strokes for N-link microswimmer," in *Proc. IEEE Conf. on Decision and Control*, 2013, pp. 3870–3875.
[35] A. H. Nayfeh, *Perturbation methods*. Willey-VCH, 2004.
[36] L. E. Becker, S. A. Koehler, and H. A. Stone, "On self-propulsion of micro-machines at low Reynolds numbers: Purcell's three-link swimmer," *J. Fluid Mech.*, vol. 490, pp. 15–35, 2003.
[37] F. Alouges, A. DeSimone, L. Giraldi, and M. Zoppello, "Self-propulsion of slender micro-swimmers by curvature control: N-link swimmers," *International Journal of Non-Linear Mechanics*, vol. 56, pp. 132–141, 2013.
[38] D. R. Mitchell, "Chlamydomonas flagella," *Journal of Phycology*, vol. 36, no. 2, pp. 261–273, 2000.
[39] B. Friedrich, I. Riedel-Kruse, J. Howard, and F. Jülicher, "High-precision tracking of sperm swimming fine structure provides strong test of resistive force theory," *The Journal of experimental biology*, vol. 213, no. 8, pp. 1226–1234, 2010.
[40] Y. Or, "Asymmetry and stability of shape kinematics in microswimmers' motion," *Physical Review Letters*, vol. 108, p. 258101, 2012.
[41] ——, "Dynamics and stability of Purcell's three-link microswimmer near a wall," *Physical Review E*, vol. 82, p. 065302(R), 2010.
[42] A. M. J. Davis and D. G. Crowdy, "Matched asymptotics for a treadmilling low-Reynolds-number swimmer near a wall," *The Quarterly Journal of Mechanics and Applied Mathematics*, vol. 66, no. 1, pp. 53–73, 2013.
[43] D. G. Crowdy and O. Samson, "Hydrodynamic bound states of a low-Reynolds-number swimmer near a gap in a wall," *Journal of Fluid Mechanics*, vol. 667, pp. 309–335, 2011.
[44] D. G. Crowdy, S. Lee, O. Samson, A. Hosoi, and E. Lauga, "A two dimensional model of low Reynolds number swimmers beneath a free surface," *Journal of Fluid Mechanics*, vol. 681, pp. 24–47, 2011.
[45] E. Passov (Gutman) and Y. Or, "Dynamics of purcells three-link microswimmer with a passive elastic tail," *The European Physical Journal E*, vol. 35, no. 8, 2012.
[46] L. J. Burton, R. L. Hatton, H. Choset, and A. E. Hosoi, "Two-link swimming using buoyant orientation," *Physics of Fluids*, vol. 22, p. 091703, 2010.
[47] E. Gutman and Y. Or, "Simple model of a planar undulating magnetic microswimmer," *Physical Review E*, vol. 90, p. 013012, 2014.